



Article

Combining MWL and MSG SEVIRI Satellite Signals for Rainfall Detection and Estimation

Kingsley K. Kumah ^{1,*}, Joost C. B. Hoedjes ¹, Noam David ², Ben H. P. Maathuis ¹,
H. Oliver Gao ³ and Bob Z. Su ¹

¹ Faculty of Geo-Information Science and Earth Observation (ITC), University of Twente, 7500 AE Enschede, The Netherlands; j.c.b.hoedjes@utwente.nl (J.C.B.H.); b.h.p.maathuis@utwente.nl (B.H.P.M.); z.su@utwente.nl (B.Z.S.)

² AtmosCell, Tel Aviv, Israel; noam@atmoscell.com

³ The School of Civil and Environmental Engineering, Cornell University, Ithaca, NY 14853, USA; hg55@cornell.edu

* Correspondence: kkumahkwabena@gmail.com

Received: 29 July 2020; Accepted: 14 August 2020; Published: 19 August 2020



Abstract: Accurate rainfall detection and estimation are essential for many research and operational applications. Traditional rainfall detection and estimation techniques have achieved considerable success but with limitations. Thus, in this study, the relationships between the gauge (point measurement) and the microwave links (MWL) rainfall (line measurement), and the MWL to the satellite observations (area-wide measurement) are investigated for (area-wide) rainfall detection and rain rate retrieval. More precisely, we investigate if the combination of MWL with Meteosat Second Generation (MSG) satellite signals could improve rainfall detection and rainfall rate estimates. The investigated procedure includes an initial evaluation of the MWL rainfall estimates using gauge measurements, followed by a joint analysis of the rainfall estimates with the satellite signals by means of a conceptual model in which clouds with high cloud top optical thickness and large particle sizes have high rainfall probabilities and intensities. The analysis produced empirical thresholds that were used to test the capability of the MSG satellite data to detect rainfall on the MWL. The results from Kenya, during the “long rains” of 2013, 2014, and 2018 show convincing performance and reveal the potential of MWL and MSG data for area-wide rainfall detection.

Keywords: rainfall detection; microwave links; satellite; MSG SEVIRI; cloud top properties

1. Introduction

Accurate rainfall detection and estimation are beneficial for many operational and research applications, including hydrological modelling, flash flood prediction, urban drainage planning, water resources management, and many more [1]. However, accurate rainfall estimation is a challenge because rainfall is intermittent and its intensities, in some cases, vary significantly in space and time [2,3]. The state-of-the-art in rainfall measurement consists of devices that can detect and quantify rainfall depending on their location [4].

Rain gauges measure rainfall accumulations as a function of time, and generally have a high degree of accuracy, especially at low to medium intensities [5]. However, rain gauges measure at a discrete point and therefore provide site-specific measurements with low spatial representativeness [6]. Interpolation techniques to obtain spatially continuous rainfall estimates from rain gauges are available, but they easily propagate errors from the point measurement and are unable to adequately capture the spatial variability of rainfall [7]. Also, installing and maintaining rain gauge networks can be practically challenging and expensive [8,9], resulting in sparse deployment and rapid decline in gauge stations, especially in developing and underdeveloped countries [10,11].

Weather radar systems usually operate at S or C-band wavelengths; with better coverage and high spatiotemporal resolution [12]. However, radar-based rainfall estimation suffers from limitations, such as ground clutter, beam blockage, attenuation due to rain, mean-field and range dependent systematic errors, see, e.g., [13–16]. Also, radars are expensive to acquire, operate and maintain, thus limiting their operation to well-funded national meteorological and hydrological services with the required technical and human resources to ensure adequate maintenance of the system and valorisation of the data in the form of relevant information products [8,17].

Alternatively, satellite systems can provide enormous and continuous rainfall data at a global scale with different spatiotemporal resolutions. Satellites estimate rainfall by remotely sensing scattered and emitted radiation from clouds, precipitation and underlying surface [18]. This can be done by visible and infrared sensors onboard geostationary satellites and passive and active microwave sensors onboard polar-orbiting satellites. Consequently, several techniques for estimating rainfall from satellites exist [19] and some of the most accurate satellite-based rainfall products, e.g., [20], incorporate in-situ measurement in the retrieval process. Nonetheless, uncertainties in satellite rainfall estimates exist at varying spatiotemporal scales [21]. In addition, for reliable application of satellite rainfall estimates, sufficient ground data are in most cases required for their evaluation at different spatiotemporal scales [22,23].

Over the past decade, a growing number of researches have shown that microwave links (MWL) from cellular communication networks can provide near ground average rainfall estimates that can complement measurements from traditional devices [23–27]. The MWL network is already existing vastly in the world, and with extensive coverage compared to rain gauges and weather radars [28]. Given its potential, the application of MWL for rainfall estimation has many benefits including (i) the possibility to estimate rainfall over large areas, especially in regions lacking traditional in-situ systems; (ii) the MWL estimates line-average rainfall, which is more representative of areal rainfall than point estimates (rain gauge); (iii) the costs related to running and maintenance of the system for rainfall monitoring are minimal. An overview of the history, theory, challenges, and opportunities of large scale rainfall monitoring using MWL is given by [29], and a review of the current status and future challenges of MWL rainfall observation can be found in [30].

Several studies have also combined different rainfall estimation methods to improve near ground rainfall estimates at different spatiotemporal scales: using rain gauge data to correct the radar rainfall estimates [31], combining radar-based areal precipitation fields with point rain gauge measurements to improve the accuracy and spatial distribution of rainfall [32], merging satellite and rain gauge [33]. A most recent example is the integrated multi-satellite retrievals from global precipitation measurement (IMERG), which incorporates monthly gauges analysis data from the Global Precipitation Climatology Centre (GPCC). Furthermore, [34–36] have all described techniques for integrating MWL, radar, and rain gauge data for improving near ground rainfall estimation and mapping.

The Meteosat Second Generation (MSG) offers the opportunity to observe the earth's atmospheric state and dynamics at $3 \times 3 \text{ km}^2$ and 15 min using a wide spectral range radiometer, namely the spinning enhanced visible and infrared imager (SEVIRI) which allows for quasi-continuous observation of rainfall distribution in near-real-time [37], and makes it possible to study convective systems that are characterized by the sudden occurrence of medium to high rainfall intensities, over small spatial scales. The individual SEVIRI spectral channels and their combinations allow for inferring cloud top properties such as optical thickness, particle size, and phase which can be used for successful rainfall detection [38,39] and estimation [37,40].

Surprisingly, the combination of MWL and MSG satellite, for rainfall detection and estimation has received far too little attention, while it could be of great value to area-wide rainfall monitoring. The combination of MWL and MSG satellite, in which MSG observes the earth's atmosphere at high spatial and temporal resolution and the MWL detects accurate near ground rainfall estimation along its path, can be the next essential step to explore the potential of MWL-satellite combination for rainfall detection and estimation. To date, Schip et al. [41] investigated the potential of MSG based satellite

rainfall product for wet and dry classification of MWL signals in the Netherlands and suggested that since the MWL estimate rainfall close to the ground, their combination with satellite data can potentially provide better estimates than a satellite-only approach. The authors of [17,42] conceptually proposed the MWL and MSG satellite data as suitable for estimating rainfall from convective systems and developing conceptual flash flood early warning system for underdeveloped countries.

The objective of this study is to investigate if the combination of MWL with MSG satellite signals could improve rainfall detection and rainfall rate estimates. Contrary to other MWL based rainfall studies, for the first time, we study the path average rainfall with the aid of signal from MSG SEVIRI channels that provides information on cloud dynamics. Our approach includes: (i) the MWL rainfall was first evaluated using rain gauge measurements; (ii) secondly, the MWL rainfall estimates were analysed as a function of the MSG SEVIRI satellite signals. The satellite signals, in this case, were used to infer information on cloud top properties, and (iii) finally, the information content gained from analyzing the MWL rainfall with MSG SEVIRI satellites signals was then used for detecting rainfall on individual MWL. This paper is organised as follows. The study area and the data used are presented in Section 2. Section 3 describes the method and performance measures used to evaluate and analyse MWL based rainfall intensities and its relationship with MSG cloud top properties. Section 4 briefly presents and discusses the results, and lastly, in Section 5, significant findings and conclusions are summarised.

2. Study Area and Dataset

2.1. Study Area

Two areas in Kenya (0.02° S, 37.90° E) were considered for this study: Kericho (0.36° S, 35.28° E) and Naivasha (-0.71° S, 36.43° E). The two locations were chosen because of the availability of MWL, rain gauge and satellite data. Located within the Kenyan Rift Valley, both study locations are dominated by farmland, and have similar rainfall patterns, with a long rainy season in the months of March, April, May, and June (“long rains”) and a shorter rainy season in October, November, and December (“short rains”) [43]. The seasonal passage of the intertropical convergence zone (ITCZ) over Kenya is known to influence both the long and short rainfall seasons [44].

The two study locations also share similar complex terrain features such as high mountains, dense forest, farmlands, water bodies and fairly populated urban areas. Kericho is characterised by hilly terrain, with elevation ranging between 1800 and 3000 m above mean sea level (a.m.s.l). Elevation in Naivasha ranges from 1980 m a.m.s.l. close to lake Naivasha to about 4000 m a.m.s.l in the Aberdare Mountains. Rainfall in both areas also varies quite noticeably with the local relief. On average, total annual rainfall varies between low and high altitudes, from 1400 to 2125 mm and 610 to 1525 mm in Kericho and Naivasha, respectively [45,46]. The temperature in Kericho ranges between 10 and 29°C [47], and in Naivasha between 8 and 30°C [46].

2.2. Data Set

This study focused on rainfall data for the “long rains” in May and June of 2013, 2014, and 2018 (Table 1). These data were obtained from MWL, rain gauges and MSG SEVIRI. Part of the data set, consisting of 2 MWL and 16 rain gauges, was used to evaluate the MWL’s capability to estimate rainfall intensities. All data were used to analyse the relationship between ground rainfall (from rain gauges and MWL rainfall estimates) and MSG satellite data for rainfall detection on MWL. The rain gauge data were considered as the reference measurement.

Table 1. Characteristics of the MWL network used in each study location.

Study Location	Evaluation Period		Number of MWL	Frequency (GHz)	Link Length (km)
	Year	Month			
Kericho	2013	May–June	2	23	<2
			4	15	3.45–4.77
			3	23	<2
Naivasha	2014	May–June	9	15	3.47–18.95
			1	8	28.4
	2018		1	15	10

2.2.1. Rain Gauge Data

Gauge rainfall data were obtained from 14 aerodynamic ‘tipping bucket’ rain gauges (ARG 100 rain gauges, see www.emltd.net) and two rain gauges from Trans-African Hydrometeorological Observatory (TAHMO) [48]. In Kericho, five ARG rain gauges were aligned near a 15 GHz, 3.68 km MWL transect during the May–June 2013 evaluation period. In Naivasha, nine ARG rain gauges were aligned under a 15 GHz, 10 km MWL, with two TAHMO gauges installed close to the transmitting and receiving antennas during the May–June 2018 evaluation period. The location of the rain gauges is shown in Figure 1, per each study location. The ARG rain gauges were set to log data every minute, while the TAHMO stations recorded rainfall every 5 min. One tip of the ARG bucket equates to 0.198 to 0.202 mm rain. No rain gauge data was used during the 2014 evaluation period due to data unavailability.

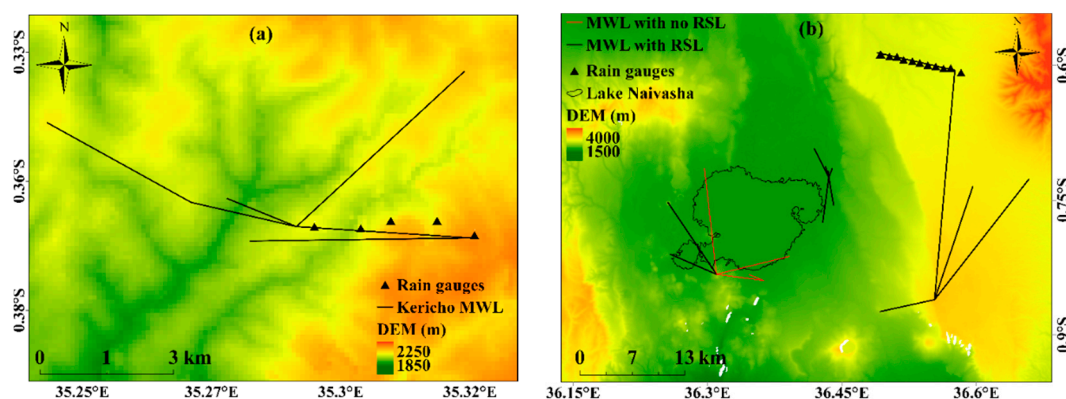


Figure 1. The locations of MWL and rain gauges in (a) Kericho and (b) Naivasha. The base map is SRTM DEM over the two study locations. Note: map coordinates are shown in decimal degrees, for some of the MWL in Naivasha no RSL data were available (red lines in (b)).

2.2.2. MWL Data

The MWL data was supplied by Safaricom, a Kenyan telecom service provider. Safaricom routinely collects and store the MWL data for monitoring purposes; access to the data is by contacting their office in Nairobi (<https://www.safaricom.co.ke/>). Received signal level (RSL) data, for the evaluation period, were acquired for a total of 19 MWL of variable lengths and frequencies. Figure 1 shows the MWL network in Kericho and Naivasha on a base map using a Shuttle Radar Topography Mission (SRTM) digital elevation model (DEM) [49]. All the MWL used were Aviat Eclipse. Table 1 gives further details on the MWL network in each study location and for each evaluation period.

The RSL data were characterized by minimum, maximum, and mean values at 15 min intervals and with a resolution of 0.1 dBm. The MWL used were vertically polarized and had constant transmitted signal levels (TSLs). Out of the 19 MWL, one link (8 GHz, 28.4 km), was not included in this study because, at such frequencies, the attenuation rainfall relationship for estimating path average rainfall is sensitive to variation in raindrop size distribution which can result in significant rainfall retrieval errors [50,51]

2.2.3. MSG Satellite Data

MSG is a successor of Meteosat First Generation (Meteosat 1–7)—a series of operational geostationary meteorological satellites that continuously observe the earth-atmosphere system. Currently, 4 Meteosat satellites (Meteosat 8, 9, 10, and 11) are positioned overhead the equator and operate over Europe, Africa and the Indian Ocean [52]. We used data from the Meteosat at 0° E (2013, 2014 evaluation periods) and 41.5° E (2018 evaluation period), which corresponded to Meteosat 10 and 8 satellite respectively [53], at the time the data were acquired. The radiometric sensor onboard MSG, SEVIRI, observes the earth's full disk in 12 spectral channels: eight thermal infrared, three solar, and one high resolution visible (HRV) channels. SEVIRI's temporal resolution is 15 min. However, the spatial resolution is 3 km for the thermal infrared and solar channels and 1 km for the HRV channel (at nadir) [54]. The data are freely available at the European Organization for the Exploitation of Meteorological Satellites (EUMETSAT) website and were imported for processing using the GEONETCast Toolbox in ILWIS (Integrated Land and Water Information System, version 3.85) [55]. We selected solar and thermal infrared channels that are sensitive to cloud top properties: optical thickness, particle size, and phase during the day and nighttime. These correspond to visible (VIS 0.6 μm), near-infrared (NIR 1.6 μm), thermal infrared (IR 3.9 μm , IR 8.7 μm , IR 10.8 μm and IR 12.0 μm), and water vapour (WV 7.3 μm) channels.

3. Method

This section includes three broad parts. Part one (Sections 3.1 and 3.2) estimates rainfall from MWL and rain gauges in Figure 1a,b. Part two (Sections 3.3 and 3.4) describes the retrieval of MSG satellite signals (for different kinds of SEVIRI channels) from the neighbourhood of MWL and gauges in part one, and analyses the data with the ground rainfall estimates. The analysis considers a combination of SEVIRI visible, near-infrared, and brightness temperature differences to infer information about cloud top properties: cloud optical thickness, particle size and phase. Although the SEVIRI based cloud properties are representative of the cloud top and has indirect and nonlinear relationship with ground rainfall [18,37], the information retrieved is useful for quantifying rainfall due to the apparent statistical relationship between rainfall duration and amount [56]. The information content gained from the joint analyses of rainfall estimates with satellite signals (for inferring cloud top properties) was then used to test the potential of the satellite data to detect rainfall on the MWL. Finally, part three (Section 3.5) presents performance measures for evaluating the MWL rainfall estimates and rainfall detection on MWL.

3.1. Estimating Rainfall from Rain Gauges

For each ARG rain gauge, the rainfall in millimetres (mm) was estimated as the tipping count multiplied by the tip equivalent of rain in mm. The rainfall in mm per minute is then used to estimate rainfall intensities $R \text{ mm h}^{-1}$ at 15 min intervals. The rainfall data from the TAHMO stations were also used to estimate rainfall intensities at 15 min to ensure temporal consistency in the gauge data. During every 15 min, the average rainfall intensities that have occurred along the MWL transmission path were calculated as the mean of the gauge rainfall estimates.

3.2. Estimating Rainfall from MWL Data

The average attenuation along the MWL path can be used to estimate the average rainfall, $R \text{ (mm h}^{-1}\text{)}$ using the formula [57]:

$$Z = aR^b \quad (1)$$

where $Z \text{ (dB km}^{-1}\text{)}$ is the rain-induced attenuation, $a \text{ ((dB km}^{-1}\text{) (mm h}^{-1}\text{)}^{-b}\text{)}$ and $b \text{ (-)}$ are empirical parameters that are known from the literature [57,58] and are dependent on MWL signal frequency and polarisation. Depending on the sampling strategy used for the MWL RSL data, different studies such as [27,59] have used different characteristics of the RSL data for rainfall estimation. Here, the RSL

data received, consisted of two instantaneous signal levels (i.e., the minimum and maximum RSL) and a mean signal level over a 15 min interval. In this study, the mean RSL was used to retrieve R to ensure a homogeneous comparison of mean rainfall estimates from rain gauges and MWL. The steps used to retrieve R from the mean RSL are briefly described below.

3.2.1. Wet/Dry Classification of RSL Data

Attenuation of MWL signal can be from sources other than rainfall. For instance, variations in water vapour content and air temperature [60,61], strong solar irradiance and multipath propagation can all cause RSL attenuation even in clear sky conditions [30]. Therefore, to estimate R from RSL data, it is essential first to identify the rain periods (wet periods, i.e., when rain is present on the MWL path) in the RSL data and separate them from the no rain periods (dry periods, i.e., when rain is absent on the MWL path). Wet/dry classification in literature is based on two major concepts. One concept assumes rainfall is correlated in space, such that neighbouring links will experience mutual attenuation during the occurrence of rain. Hence, wet/dry classification is achieved for a particular link by comparing its attenuation measurement with several links within its vicinity [27]. The other concept analyses the statistical properties of the time series of link signals, see [62] and [63].

Rainfall varies considerably in space and time over the study area [64,65]. Therefore, a wet/dry classification based on mutual attenuation of nearby links might not be a practical approach in our study location. Thus, the approach adopted in this study is based on the latter concept. For every 10 mean RSL data (the equivalent of 150 min interval), a standard deviation was estimated as a measure of the local variability in the RSL. Since rain attenuates MWL signals, the standard deviation for a rainy interval will be high. Thus, a suitable threshold value was defined to separate the standard deviation values into wet/dry periods. As proposed by [62], such a value can be derived from the rainfall climatology of the area as inferred from, e.g., nearby rain gauges. Here, the threshold value was calibrated for each study location using the experimental links and rain gauge data (Figure 1, the MWL with gauges underneath their transects). The threshold value was then applied to all the links in the respective locations, for wet/dry classification, assuming that the rainfall climatology is homogeneous for the small study location considered (Figure 1). When a 150 min interval had less than five mean RSL data, wet/dry classification and hence rainfall was not computed for that interval.

3.2.2. Estimating the Reference RSL

The reference RSL or the baseline level is an indication of the RSL levels during dry periods. According to, e.g., [27,51], accurate wet/dry classification is relevant for precise estimation of this parameter. Nevertheless, the baseline level fluctuates even in the dry period due to signal attenuations in clear sky conditions, e.g., [60,66]. For every 15 min labelled as a wet period, the corresponding baseline level was estimated as the median of the mean RSL from the previous 24 h, that was labelled as dry period.

3.2.3. Estimating R from Z

After classifying the mean RSL data into wet and dry periods, and subsequently estimating a baseline level, the effect of antenna wetting was taken into account by following the dynamic model described in [67]. Eventually, the path average attenuation, Z (dB km⁻¹), was estimated for every 15 min wet period by subtracting the mean RSL from the baseline level, as shown in Equation (2). In some cases, negative values of path average attenuation were retrieved. This is the case when a 15 min period within a 150 min interval labelled as wet is however dry because rainfall was intermittent in the wet interval. In these cases, the attenuation was set to zero.

$$Z = \frac{Pref - P}{L} \quad (2)$$

where L is MWL length (km), while P_{ref} and P (dBm) are the reference and mean RSL (corrected from the effect of wet antenna), respectively. Finally, R (mm h^{-1}) is estimated from Z via Equation (3) below

$$R = \left(\frac{Z}{a} \right)^{\frac{1}{b}} \quad (3)$$

The values of a and b were chosen from [58], and are shown in Table 2.

Table 2. a and b parameters used for estimating R from Z .

Frequency (GHz)	Parameter	
	a	b
15	0.05008	1.0440
23	0.1284	0.9630

3.3. SEVIRI Data Retrieval and Processing

The MSG SEVIRI data were retrieved for the earth's full disk for the evaluation period. The zenith viewing angle of the Meteosat at 0° E, over the study area, is approximately 41° . As a result, depending on the location and the height of clouds, this viewing angle could cause displacement of cloud tops from their actual position due to the effect of parallax, which occurs because SEVIRI observes the Earth under an oblique angle [40]. According to [17], for very high clouds in Kenya, parallax displacement can amount to about 12 km in SEVIRI pixels. Therefore the data for the 2013 and 2014 evaluation period (retrieved from Meteosat at 0° E) were parallax corrected using a correction algorithm from EUMETSAT (see http://www.essl.org/cwg/?page_id=165). However, the zenith viewing angle of the Meteosat at 41.5° E is about 5° , and this small viewing angle does not require parallax correction.

3.3.1. The Conceptual Model for Detecting Rainfall Using MSG SEVIRI Data

In this study, MWL rainfall estimates are linked to MSG SEVIRI data based on the assumption that clouds that rain over MWL can be detected (based on their cloud top properties) using the MSG SEVIRI data. A conceptual model was therefore defined that explored the relationship between spectral characteristics of different kinds of SEVIRI channels and cloud top properties (cloud top optical thickness, particle size and phase) for detecting rainfall. The model assumes that clouds with high optical thickness and large particle sizes (with the existence of ice or water hydrometeors at the top) have high rainfall probability, and intensity whereas clouds with low optical thickness and small particles sizes have low rainfall probability and intensity [37–39,68]. The physical basis underlying this assumption is that the conditions for the development of precipitation in clouds are (i) availability of sufficient moisture (ii) existence of an effective mechanism for converting small cloud droplets that are suspended in the air into large precipitating particles, and (iii) the existence of ice phase clouds at the cloud top to support rain generation by the Bergeron–Findeisen process [39,69–71].

MSG SEVIRI based operational cloud property retrieval technique applicable to water and ice clouds is not available [37,39]. Nonetheless, many authors, including [37,69,72–74] have shown that implicit information about the cloud top properties indicated above can be inferred from solar and thermal infrared satellite channels. For this reason, this study utilized the original reflectance and brightness temperature differences of SEVIRI channels to infer cloud top properties for detecting rainfall. Because the information about cloud properties differs between day and nighttime, the detection of raining clouds is done separately for day and nighttime. To be sure that only cloudy scenes are used in this analysis, EUMETSAT's operational cloud mask product [75] was used to identify cloudy pixels.

(i) Detecting raining clouds during daytime

Reflection of solar radiation by clouds in the non-absorbing channels (i.e., in the visible channels between $0.4 \mu\text{m}$ and $0.8 \mu\text{m}$) is strongly related to the cloud optical thickness, and that of the solar

radiation in the slightly absorbing channels (1.6 μm and 3.9 μm) is related to the particle size [76–78]. The two kinds of channels combined can, therefore, provide information about cloud optical thickness and particle size. The optical thickness and particle size of clouds both represent a single parameter, cloud water path (CWP), and is directly related to rainfall probability of clouds. The CWP is an indicator of the amount of water vertically integrated into the cloud. It depends on the diameter of particle size and the thickness of clouds formed by these particles [72,73,79].

Consequently, CWP is often implicitly inferred from VIS 0.6 μm and NIR 1.6 μm channels from SEVIRI [39,80]. High VIS 0.6 μm reflectance indicates optically thick clouds and low NIR 1.6 μm reflectance corresponds to large cloud particle sizes. The implication is that large CWP is observed when high VIS 0.6 μm reflectance coincides with low NIR 1.6 μm reflectance. In [39], clouds with large CWP were found to coincide with high rainfall probabilities, when their SEVIRI reflectance was compared with weather radar data.

The difference in brightness temperature between IR 8.7 μm and 10.8 μm ($\Delta T_{\text{IR}8.7\text{-IR}10.8}$) and that between IR 10.8 μm and 12.0 μm ($\Delta T_{\text{IR}10.8\text{-IR}12.0}$), can be used to infer information about cloud phase [39]. Based on the observations made by [81], water particle absorption is stronger between 11 μm and 12 μm than between 8 μm and 11 μm , whereas the reverse is true for ice particle. Thus, $\Delta T_{\text{IR}10.8\text{-IR}12.0}$ of water clouds are higher than $\Delta T_{\text{IR}8.7\text{-IR}10.8}$. On the contrary, $\Delta T_{\text{IR}8.7\text{-IR}10.8}$ of ice clouds is higher than coincident $\Delta T_{\text{IR}10.8\text{-IR}12.0}$. [82] have rather suggested the simultaneous use of brightness temperature IR10.8 μm ($T_{\text{IR}10.8}$) and the difference $\Delta T_{\text{IR}8.7\text{-IR}10.8}$ for identifying cloud phase. Their study found that ice crystals begin to form when $T_{\text{IR}10.8} < 238 \text{ K}$ and $\Delta T_{\text{IR}8.7\text{-IR}10.8} > 0.25 \text{ K}$. As earlier indicated, the existence of ice phase at the cloud top, supports rain generation and thus increases the likelihood of a cloud to produce rain. The $\Delta T_{\text{IR}10.8\text{-IR}12.0}$ has also been considered as a good indicator of cloud optical thickness, and is effective for discriminating optically thick cumulus clouds from optically thin cirrus clouds [74,83,84]. According to [85], optically thick cumulus clouds show small $\Delta T_{\text{IR}10.8\text{-IR}12.0}$ because of their black-body characteristics while optically thin cirrus clouds show larger difference because of the differential absorption between of ice crystals between the two channels. It is expected that optically thick cumulus-type clouds with small $\Delta T_{\text{IR}10.8\text{-IR}12.0}$ produce rain [83]. Although $\Delta T_{\text{IR}10.8\text{-IR}12.0}$ is effective in detecting and removing optically thin cirrus clouds, [86] found instances where optically thick cumulus-type clouds were incorrectly classified as optically thick cirrus clouds.

(ii) Detecting raining clouds during nighttime

During the nighttime, the brightness temperature differences: $\Delta T_{\text{IR}3.9\text{-IR}10.8}$, $\Delta T_{\text{IR}3.9\text{-WV}7.3}$, $\Delta T_{\text{IR}8.7\text{-IR}10.8}$, and $\Delta T_{\text{IR}10.8\text{-IR}12.0}$ were used to infer information about cloud optical thickness, particle size and phase [38,69,71,80] for rainfall detection. As explained by [38,80], the emissions in 3.9 μm are sensitive to particle size, such that large particles have high emissions than smaller particles. The dependence on particle size is less distinct in the IR10.8 μm than in IR3.9 μm . As a result, $\Delta T_{\text{IR}3.9\text{-IR}10.8}$ values are higher for large particle sizes compared to smaller particles. Using $\Delta T_{\text{IR}3.7\text{-IR}11}$ of TRMM satellite, [69] showed that optically thick raining clouds with large particles produced brightness temperature difference in the interval -1 to 4 K . Concerning the $\Delta T_{\text{IR}3.9\text{-WV}7.3}$ difference, [38] indicated that the characteristics should be similar to $\Delta T_{\text{IR}3.9\text{-IR}10.8}$ but with generally higher differences than $\Delta T_{\text{IR}3.9\text{-IR}10.8}$. This is due to the diminishing effect of the water vapour absorption and emission in the mid-to-low tropospheric levels on the brightness temperature in WV7.3 μm channel [54]

3.3.2. The Spatial and Temporal Differences between SEVIRI and Ground Data

The measurement characteristics of satellite and ground sensors are fundamentally different [87]. The satellite measures instantaneously over a wide area, while the ground sensors measure continuously in time from a single location (rain gauges), or aggregated measurements over time and space (MWL). The measurement differences, therefore, suggest a possible spatial and temporal mismatch between satellite and ground measurements that must be taken into account when analysing the two datasets.

The description below presents the spatial and temporal difference between the SEVIRI and ground sensors (MWL or rain gauges) together with how they are treated in this study.

(i) Spatial mismatch

The general assumption required for a comparison of ground rainfall and satellite data is that the measured rainfall is representative of the whole satellite pixel containing the ground sensors. In addition to the above-mentioned measurement mismatch, it has been shown that, for a heavy rain with hydrometeors falling out of a cloud in the height of 3 km, at a falling speed of 10 ms^{-1} and horizontal wind speed between 5 and 30 ms^{-1} , the hydrometeors can drift a horizontal distance anywhere between 1.5 and 90 km [88]. Thus, the rainfall recorded by a ground sensor might not correlate with the satellite signal from a collocated pixel but with the signal from other adjacent pixels. Furthermore, for tropical deep convective systems consisting of convective cores and anvil cloud areas having different cloud properties, dynamical regimes, and varying rainfall intensities, the retrieved cloud top properties might be biased towards the spatially dominant anvil cloud areas [89].

To minimise the effect of the above potential spatial mismatches between the satellite and ground data in our analysis, an approach is adopted that considers not only the pixel containing the ground sensor but also the surrounding three by three pixels. This implies that for a rain gauge, the surrounding three by three pixels of the pixel containing the gauge were considered and for the MWL, three by three pixels surrounding the centre of the MWL transect were considered. It is worth noting that, by including three by three pixels surrounding the centre of the link, all the pixels covering the MWL are also included in the analysis.

Two different spatial aggregation methods (i.e., summary statistics used to sample from the raw data in space) were used to retrieve a single satellite signal out of the three by three pixel environment that can be compared to the ground rainfall. For day time data, the method previously described by [37] was used because of its simplicity, and effectiveness in identifying the most effective satellite signal that can be analysed with the ground rainfall data. The method identifies the pixel with the most effective satellite signal as the pixel with the highest reflectance value in the VIS $0.6 \mu\text{m}$ (indicating high optical thickness, i.e., thick clouds) and lowest reflectance values in the NIR $1.6 \mu\text{m}$ (indicating large particle size). More precisely, for $n \geq 2$ (where n is the number of cloudy pixels in the three by three pixels environment) the maximum and minimum reflectance values were expressed as:

$$VIS_{ref} = \max_{i=1,n}(x_i) \quad (4)$$

where x_i is the reflectance value in the VIS $0.6 \mu\text{m}$ channel, and

$$NIR_{ref} = \min_{i=1,n}(y_i) \quad (5)$$

where y_i is the reflectance value in the NIR $1.6 \mu\text{m}$ channel. In case the retrieved maximum VIS $0.6 \mu\text{m}$ and minimum NIR $1.6 \mu\text{m}$ values do not occur in the same pixel, the value combination that returns the highest difference between the two signals is used. The maximal difference was expressed as:

$$MaxDiff_{VISNIR} = \max_{i=1,n}(x_i - y_i) \quad (6)$$

The approach theoretically assumes that, by identifying the pixel with the maximum reflectance in VIS $0.6 \mu\text{m}$, the pixel with the highest optical thickness is detected. For the NIR $1.6 \mu\text{m}$ reflectance, by identifying the pixel with the minimum reflectance, the pixel with the largest effective particle size is detected. Thus, the pixel with the highest optical thickness, large particle size, and the corresponding large CWP is detected. Once the cloudy pixel with large CWP is detected, the phase of clouds is then retrieved using $\Delta T_{IR8.7-IR10.8}$ and $\Delta T_{IR10.8-IR12.0}$. By using this method, the satellite pixel with the most effective rainfall signal is identified and retrieved for analysis with the ground rainfall data.

However, for nighttime, the mean of brightness temperature differences retrieved from cloudy scenes was analysed with the ground rainfall. The mean brightness temperature differences for $n \geq 2$ (where n is the number of cloudy pixels in the three by three pixels environment) was expressed as:

$$Mean = \frac{1}{n} * \sum_{i=1}^n \Delta T_i \quad (7)$$

where ΔT_i is the brightness temperature difference for the various channel combinations considered.

(ii) Temporal mismatch

The potential temporal mismatch between the satellite and ground data is mainly because SEVIRI instantaneous scenes over the study area are acquired in about 6 min (depending on the latitude) into each 15 min scan interval. Therefore, the measurement might be representative of the cloud top conditions that were available during the first few minutes of SEVIRI's 15 min scan interval. In contrast, the ground measurements were continuous in time. In particular, the gauges originally recorded data at least every minute, while the MWL recorded mean RSL every 15 min (Section 2.2). Moreover, during a 15 min interval, a raining cloud could have passed over the ground sensor during the first 6 min (when SEVIRI scenes were available) or the last 9 min. Thus, the satellite measurement might not necessarily coincide with the ground measurement in time. To minimise the effect of this temporal mismatch in our analysis, the dataset was aggregated in time. This implies that, for the satellite data, the mean satellite signal was computed and for the ground data, the rainfall sums were computed every 30 min.

Other measurement characteristics of the satellite that can potentially cause uncertainties in the analysis of the ground and satellite data are the effect of viewing and illumination geometries: solar zenith angle, viewing zenith, and relative azimuth angles [90]. These effects concern the data (for periods in 2013 and 2014) acquired from solar channels of the Meteosat at 0° E. Since small study locations are considered (Figure 1) in this study, the effects of viewing and illuminating geometries should be minimal. Additionally, we only used solar reflectance for daytime hours when sufficient solar illumination was available over the study area.

3.4. Analysing MWL Rainfall and SEVIRI Data

The ground rainfall and satellite data were analysed separately for both day and night using rainfall data from the experimental setup in Figure 1, and SEVIRI satellite signals retrieved (for different channels) from the neighbourhood of the setup. The rainfall data were aggregated in time, and satellite data was aggregated in both space and time to reduce the effect of measurement discrepancies between the satellite and ground sensors (see above for details). The collocated ground rainfall and satellite data allowed us to separate raining from non-raining satellite signals. The raining satellite signals were further classified based on different rainfall categories to investigate the satellite signals for varying rainfall intensity ranges. The rainfall classes were determined by analysing the frequency distribution of the gauge rainfall intensities (not shown in this study) and using the following criteria if possible: (1) each rainfall class should have sufficient amount of data to enable the computation of some descriptive statistics; (2) the rainfall classes should be equal for both study locations to ensure homogenous rainfall analysis across the two areas.

A scatter plot of rainfall intensities as a function of the retrieved satellite signals for different combination of SEVIRI channels (that provide information about cloud top properties) was used to investigate rainfall occurrences in each rainfall class and the corresponding values in the satellite signal. The satellite signals for each rainfall class was statistically analysed using descriptive statistics.

Based on the statistical information, the potential of combining the information content from the different kinds of SEVIRI channels to detect rainfall occurrences on individual MWL was further tested. Rainfall occurrences are inferred from joint analysis of satellite and rainfall data [74,91] by

evaluating, at each timestamp, a four-dimensional matrix of VIS 0.6, NIR 1.6, $\Delta T_{IR8.7-IR10.8}$, $\Delta T_{IR10.8-IR12.0}$ (during day time), and $\Delta T_{IR3.9-IR10.8}$, $\Delta T_{IR3.9-WV7.3}$, $\Delta T_{IR8.7-IR10.8}$, $\Delta T_{IR10.8-IR12.0}$ (during nighttime) to make a rain or no-rain decision. The rain detection test was conducted using independent MWL and satellite dataset. All cloudy pixels that were considered for analysis based on the conceptual model (Section 3.3.1) were used in evaluating the capability of the test to detect rain occurrence on individual MWL.

3.5. Performance Measures

3.5.1. Evaluating MWL Rainfall Intensities

The MWL rainfall estimates (R_{MWL}) were evaluated against the rain gauge estimates (R_{RG}) using the relative bias (RB), coefficient of variation (CV), coefficient of determination (r^2), and root mean square error (RMSE) (see Table 3).

Table 3. Performance measures for evaluating R_{MWL} . Full name of each measure is indicated in the text. j and n represent all timestamps for the evaluation period.

Performance Measure	Formula	Range
RB	$\frac{\frac{1}{n} \sum_{j=1}^n (R_{MWL} - R_{RG})}{\frac{1}{n} \sum_{j=1}^n R_{RG}}$	-1 to $+\infty$
CV	$\frac{\sqrt{Var(R_{MWL} - R_{RG})}}{\frac{1}{n} \sum_{j=1}^n R_{RG}}$	0 to ∞
r^2	$\left[\frac{Cov(R_{MWL}, R_{RG})}{S_{R_{MWL}} * S_{R_{RG}}} \right]^2$	0 to 1
RMSE	$\sqrt{\frac{1}{n} \sum_{j=1}^n (R_{MWL} - R_{RG})^2}$	0 to $+\infty$

Note: Var is the variance, Cov is the covariance of the R_{MWL} , and the R_{RG} and S is the standard deviation.

RB indicates whether the R_{MWL} systematically over or underestimates the R_{RG} [92], and ranges from -1 to $+\infty$, with 0 being an unbiased case. The CV indicates how the R_{MWL} varies around the mean of the R_{RG} [5], and ranges from 0 to ∞ . The r^2 shows the strength of the linear relationship between the R_{MWL} and the R_{RG} . It ranges from 0 to 1, where 1 indicates a perfect linear correlation between the R_{MWL} and the R_{RG} [93]. Finally, the RMSE shows how close the R_{MWL} is to R_{RG} and ranges from 0 to positive ∞ , where 0 is a hypothetical case, and larger RMSE indicates decreasing accuracies of R_{MWL} [93,94]. All the performance measures were computed across the evaluation period.

3.5.2. Evaluating the Performance of SEVIRI Based Rain Detection on MWL

The performance of the rain detection test was evaluated by computing the values of a , b , c and d as described in [93,95]. The formulation of these elements differs for day and nighttime because of the different SEVIRI channels and information content used for each time of the day (i.e., day or nighttime). For daytime, a_d , b_d , c_d , and d_d were computed as:

$$a_d = R_{sat} \left(\begin{array}{l} Vis \geq Vis_{thres} \text{ AND } Nir \leq Nir_{thres} \text{ AND } \\ \Delta T_{\beta 1} \in [x_1, x_2] \text{ AND } \Delta T_{\beta 2} \in [y_1, y_2] \end{array} \right) \text{ AND } (R_{MWL} \geq 1 \text{ mmh}^{-1}) \quad (8)$$

$$b_d = noR_{sat} \left(\begin{array}{l} Vis < Vis_{thres} \text{ AND } Nir > Nir_{thres} \text{ AND } \\ \Delta T_{\beta 1} \notin [x_1, x_2] \text{ AND } \Delta T_{\beta 2} \notin [y_1, y_2] \end{array} \right) \text{ AND } (R_{MWL} \geq 1 \text{ mmh}^{-1}) \quad (9)$$

$$c_d = R_{sat} \left(\begin{array}{l} Vis \geq Vis_{thres} \text{ AND } Nir \leq Nir_{thres} \text{ AND } \\ \Delta T_{\beta 1} \in [x_1, x_2] \text{ AND } \Delta T_{\beta 2} \in [y_1, y_2] \end{array} \right) \text{ AND } (R_{MWL} < 1 \text{ mmh}^{-1}) \quad (10)$$

$$d_d = noR_{sat} \left(\begin{array}{l} Vis < Vis_{thres} \text{ AND } Nir > Nir_{thres} \text{ AND } \\ \Delta T_{\beta 1} \notin [x_1, x_2] \text{ AND } \Delta T_{\beta 2} \notin [y_1, y_2] \end{array} \right) \text{ AND } (R_{MWL} < 1 \text{ mmh}^{-1}) \quad (11)$$

where: a_d , b_d , c_d , and d_d are the hits, misses, false alarms and correct negatives events respectively; R_{sat} and noR_{sat} are raining and non-raining conditions in the satellite data; Vis , Nir , are VIS 0.6 μm and NIR 1.6 μm as well as their respective thresholds Vis_{thres} and Nir_{thres} ; $\Delta T_{\beta 1}$, $\Delta T_{\beta 2}$ are $\Delta T_{IR10.8-IR12.0}$ and $\Delta T_{IR8.7-IR10.8}$ and their brightness temperature ranges $[x_1, x_2]$ and $[y_1, y_2]$, respectively. During the nighttime, the corresponding values of a_n , b_n , c_n , and b_n were computed as:

$$a_n = R_{sat} \left(\begin{array}{l} \Delta T_{\gamma 1} \in [u_1, u_2] \text{ AND } \Delta T_{\gamma 2} \in [v_1, v_1] \text{ AND} \\ \Delta T_{\beta 1} \in [x_1, x_2] \text{ AND } \Delta T_{\beta 2} \in [y_1, y_2] \end{array} \right) \text{ AND } (R_{MWL} \geq 1 \text{ mmh}^{-1}) \quad (12)$$

$$b_n = noR_{sat} \left(\begin{array}{l} \Delta T_{\gamma 1} \notin [u_1, u_2] \text{ AND } \Delta T_{\gamma 2} \notin [v_1, v_1] \text{ AND} \\ \Delta T_{\beta 1} \notin [x_1, x_2] \text{ AND } \Delta T_{\beta 2} \notin [y_1, y_2] \end{array} \right) \text{ AND } (R_{MWL} \geq 1 \text{ mmh}^{-1}) \quad (13)$$

$$c_n = R_{sat} \left(\begin{array}{l} \Delta T_{\gamma 1} \in [u_1, u_2] \text{ AND } \Delta T_{\gamma 2} \in [v_1, v_1] \text{ AND} \\ \Delta T_{\beta 1} \in [x_1, x_2] \text{ AND } \Delta T_{\beta 2} \in [y_1, y_2] \end{array} \right) \text{ AND } (R_{MWL} < 1 \text{ mmh}^{-1}) \quad (14)$$

$$d_n = noR_{sat} \left(\begin{array}{l} \Delta T_{\gamma 1} \notin [u_1, u_2] \text{ AND } \Delta T_{\gamma 2} \notin [x_2, y_2] \text{ AND} \\ \Delta T_{\beta 1} \notin [x_1, x_2] \text{ AND } \Delta T_{\beta 2} \notin [y_1, y_2] \end{array} \right) \text{ AND } (R_{MWL} < 1 \text{ mmh}^{-1}) \quad (15)$$

where: a_n , b_n , c_n , and d_n are the hits, misses, false alarms and correct negatives events respectively during the nighttime; $\Delta T_{\gamma 1}$ and $\Delta T_{\gamma 2}$ are $\Delta T_{IR3.9-IR10.8}$, $\Delta T_{IR3.9-WV7.3}$ and their brightness temperature ranges $[u_1, u_2]$, and $[v_1, v_1]$, respectively.

With the computation of these values, a set of standard verification scores: the probability of detection (POD), false alarm ratio, (FAR), probability of false detection (POFD), accuracy (ACC), critical success index (CSI), and Heidke skill score (HSS) were computed. POD is used here to evaluate the fraction of the R_{MWL} that was correctly detected by the test $\left(\text{POD} = \frac{a}{a+b} \right)$. FAR answered the question, ‘what fraction of the number of R_{MWL} detected by the test was incorrect?’ $\left(\text{FAR} = \frac{a}{a+c} \right)$. POFD indicates the fraction of no rain ($R_{MWL} < 1 \text{ mm h}^{-1}$) on the MWL that was incorrectly identified as rain ($R_{MWL} > 1 \text{ mm h}^{-1}$) by the test $\left(\text{POFD} = \frac{c}{c+d} \right)$. The overall fraction of rain and non-rain that was correctly detected by the test was evaluated by the ACC $\left(\text{ACC} = \frac{a+d}{a+b+c+d} \right)$. CSI is used to show how well the rain detected by the test corresponds to R_{MWL} on individual MWL $\left(\text{CSI} = \frac{a}{a+b+c} \right)$. The HSS evaluates the accuracy of the rain detection test by taking into account the detection that was due to random chance.

It is calculated as:

$$\text{HSS} = \frac{(a+d) - (a_{\text{random}})}{N - a_{\text{random}}} \quad (16)$$

where $a_{\text{random}} = \frac{(a+b) \times (a+c) + (d+b) \times (d+c)}{N}$ and N is the sum of a , b , c and d .

4. Results and Discussion

4.1. Results

The first part of this section presents the results of evaluating the MWL rainfall against gauges measurements. The second part shows the results of analyzing the rainfall estimates in part 1 with the SEVIRI satellite signals for rainfall detection. The final part summarizes the performance of the satellite data when used to detect rainfall on MWL.

4.1.1. R_{MWL} versus R_{RG}

The rainfall estimates evaluated in this section were from the experimental setup in Figure 1 (i.e., the MWL with gauges under their transects). The period for which the rainfall intensities were evaluated was during the long rains of 2013 and 2018 for the Kericho and Naivasha setup respectively. The frequency of both links is 15 GHz, and their lengths are approximately 3.7 and 10 km for the

Kericho and Naivasha MWL respectively. The MWL rain estimates were evaluated using 16 rain gauges; 5 for the Kericho link and 11 for the Naivasha link. Here, the gauge rainfall intensities were considered as the reference rainfall measurement.

The transformation of MWL RSL to R_{MWL} is compared with R_{RG} for both Kericho and Naivasha in Figures 2 and 3, respectively. The comparison was made at 15 min interval using 48 h of gauge and MWL measurements.

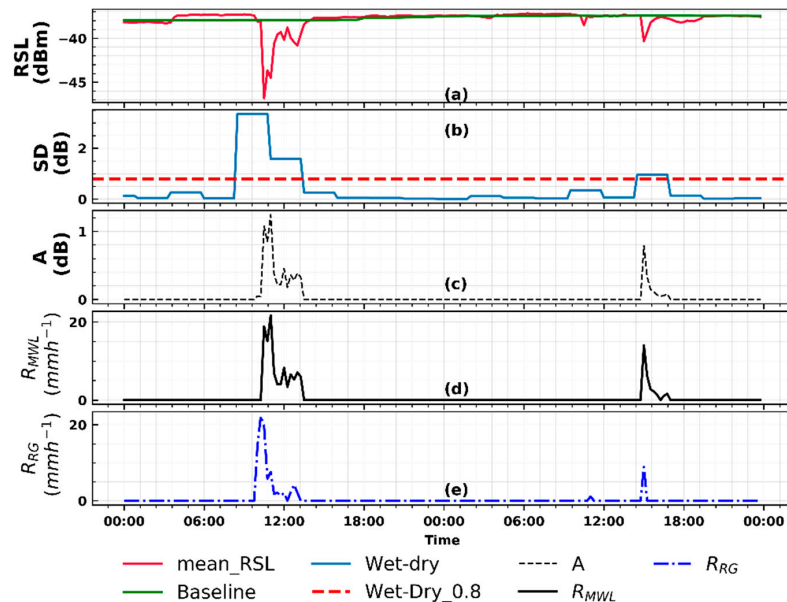


Figure 2. From raw RSL to rainfall using MWL data from Kericho, on 11 May 2013 to 12 May 2013. (a) mean and reference RSL (b) rolling standard deviation with a threshold of 0.8 dB for detecting wet/dry periods (c) attenuation (d) MWL derived rainfall intensities, and (e) rain gauge derived rainfall intensities.

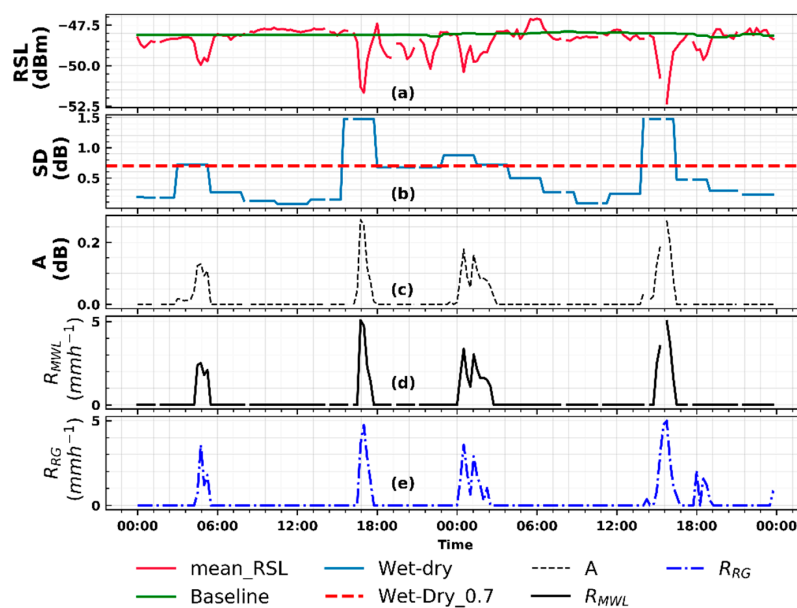


Figure 3. From raw RSL to rainfall using MWL data from Naivasha, on 4 June 2018 to 5 June 2018. (a) mean and reference RSL (b) rolling standard deviation with a threshold of 0.7 dB for detecting wet/dry periods (c) attenuation (d) CML derived rainfall intensities (e) rain gauge derived rainfall intensities.

The Naivasha link (Figure 3a) had frequent intermittent periods of no data compared to the Kericho link (Figure 2a). The data gaps were considered during the MWL rainfall estimation procedure (see Section 3.2). The estimated threshold for wet/dry classification using a rolling standard deviation method was 0.8 dB for Kericho and 0.7 dB for Naivasha (Figures 2b and 3b). Comparatively, rain detection in the Kericho link was better than in the Naivasha link.

The R_{MWL} and R_{RG} are also compared in a scatter plot at 15 min, half-hourly and hourly evaluation timestamps for both study locations (Figure 4). The half-hourly and hourly values were computed by summing the 15 min rainfall intensities. The values of the performance measures are also summarised in Table 4 for each evaluation timestamp and study location. For the scatter plot comparison and computation of the performance measures, R_{MWL} and R_{RG} pairs that are less than 1 mm h^{-1} , were set to 0 mm h^{-1} (i.e., considered as dry). However, data with the 0 mm h^{-1} were included in all analysis to evaluate the MWL's detection and estimation capabilities for both wet and dry periods. All performance measures were computed across each evaluation period.

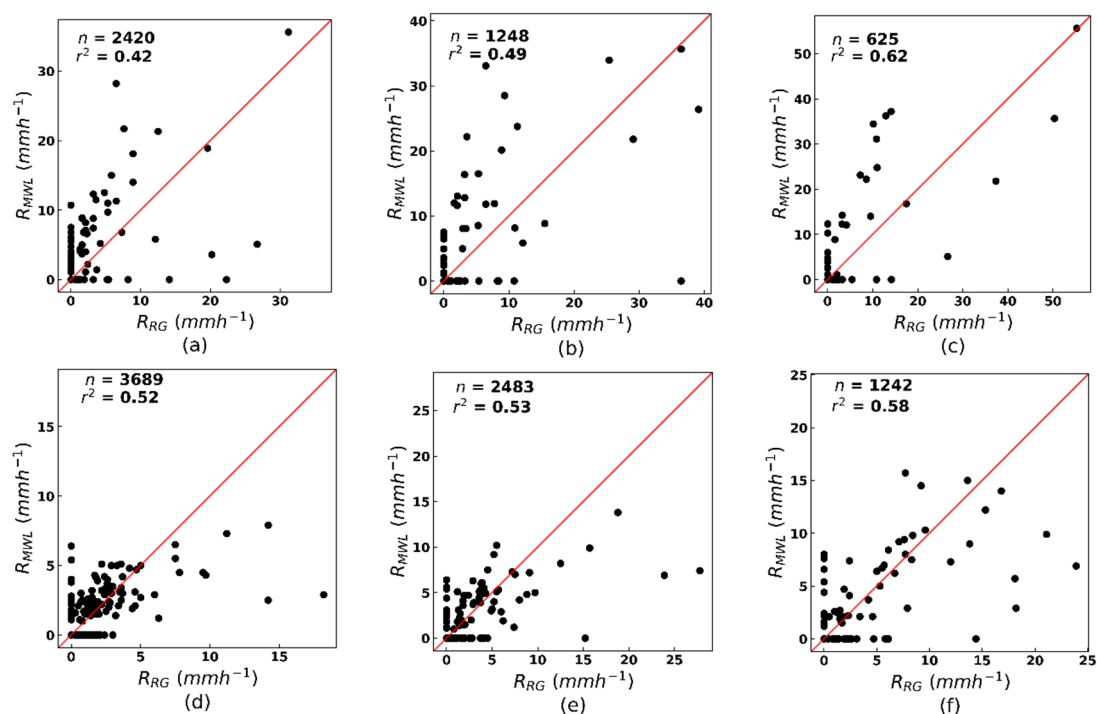


Figure 4. Scatter plot comparison of R_{MWL} and the R_{RG} for Kericho (a–c) and Naivasha (d–f) at 15 min (a,d), half-hourly (b,e) and hourly (c,f) timestamp.

Table 4. Performance measures calculated from R_{MWL} and R_{RG} pairs from the two study locations.

Study Location	RB			CV			r^2			RSME (mm h^{-1})		
	15 min	30 min	1 h	15 min	30 min	1 h	15 min	30 min	1 h	15 min	30 min	1 h
Kericho ¹	0.50	0.32	0.32	9.87	7.18	5.09	0.42	0.49	0.62	1.22	1.96	2.77
Naivasha ²	−0.05	−0.14	−0.18	5.78	5.68	4.07	0.52	0.53	0.58	0.48	0.80	1.15

¹ Performance measures were computed using 26 days of R_{MWL} and R_{RG} pairs. ² performance measures were calculated using 52 days of R_{MWL} and R_{RG} pairs.

Regarding the accuracy of the R_{MWL} , both links exhibited different skill, when their R_{MWL} were compared to the R_{RG} . As can be seen from Table 4, the link in Kericho overestimated the observed rainfall. The overestimation, however, decreased at increasing aggregation timestamp. The RB decreased from 0.50 at the 15 min timestamp to 0.32 for both half-hourly and hourly timestamps. Likewise, the CV decreased from 9.87 at 15 min to 5.09 at the hourly timestamp. The strength of the relationship between R_{MWL} and R_{RG} (see also Figure 4a–c) increased for increasing timestamps, with r^2 values reaching approximately 0.6 at the hourly timestamp. The RMSE, however, increased from 1.22 mm h^{−1} at 15 min to 2.77 mm h^{−1} at the hourly timestamps.

In contrast, the link in Naivasha (Table 4) marginally underestimated the observed rainfall. The value of RB increased minimally from −0.05 at 15 min to −0.18 at half-hourly and hourly timestamps. The CV decreased from 5.78 to 4.07 for 15 min to hourly evaluation timestamps. The strength of the relationship between R_{MWL} and R_{RG} (Figure 4d–f) also increased for increasing timestamp with r^2 above 0.5 for all timestamps. Even though the RMSE increased with aggregation time, the values (Table 4) were comparatively lower than those of the Kericho link.

4.1.2. Joint Analysis of Rainfall and SEVIRI Satellite Data

In this section, the results of analysing rainfall estimates with SEVIRI satellite data are presented in two parts. First, collocated ground rainfall (from MWL and rain gauge) and satellite data from the experimental setup in Figure 1a,b were jointly analysed for detecting rainfall. The gauge rainfall intensities presented in this analysis were from the rain gauges close to the centre of each MWL. Note, however, that the inclusion of the gauge rainfall data gave a perspective of the rainfall satellite analysis from a reference measurement point of view. To further investigate the satellite signals for different rainfall intensity ranges, the rainfall values were grouped into different rain classes (Table 5). The analysis was done separately for the two study areas and for during day and nighttime. Next, inferences deduced from the rainfall satellite analysis are summarised based on observations from the two study areas and separately for during day and nighttime.

Table 5. Summary of the R_{MWL} data per each study area for the day and nighttime.

Study Area	R_{MWL} (mm h ^{−1})	¹ Percentage of Data (%)		Accumulated R_{MWL} (mm)	
		Day	Night	Day	Night
Kericho	0	91.56 (93.81)	94.5 (97.7)	0 (0)	0 (0)
	0–5	1.95 (2.61)	2.29 (1.84)	12.22 (24.92)	13.57 (12.06)
	>5	6.49 (3.58)	3.21 (0.46)	314.25 (219.49)	98.1 (39.40)
Naivasha	0	96.68 (96.84)	95.34 (96.02)	0 (0)	0 (0)
	0–5	2.41 (2.11)	2.61 (2.88)	48.45 (34.74)	61.92 (54.14)
	>5	0.90 (1.05)	2.06 (1.1)	43.02 (88.88)	106.09 (61.41)

Note: ¹ values used in calculating percentages in Kericho and Naivasha are: 307, 217; 663, 729 for day and nighttime, respectively; values in parenthesis are computed based on the rain gauge data.

(i) MSG satellite rainfall

Figure 5 is a scatter plot of rainfall intensities as a function of the MSG satellite signals during the daytime in May–June 2013 (in total 313 MSG SEVIRI scenes). A clear observation from the figure is the difference in the scatter of data points between the raining satellite signals (0–5 mm h^{−1} and above 5 mm h^{−1} rainfall classes) and non-raining satellite signals (0 mm h^{−1} rainfall class). This feature was evident in both reflectance and brightness temperature difference combination, as well as from both the R_{RG} and R_{MWL} scatter plots.

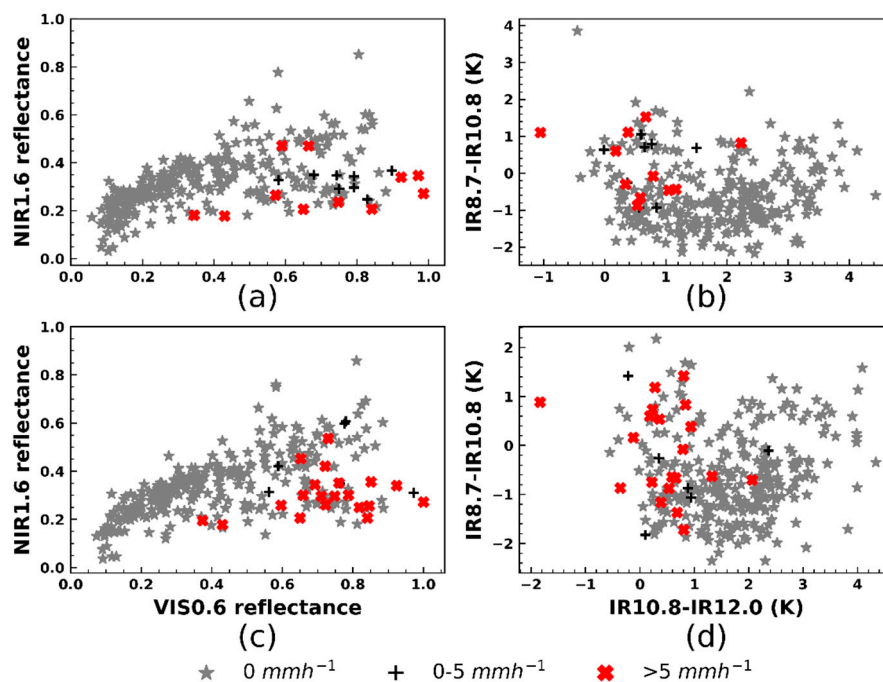


Figure 5. Day time R_{RG} (a,b) and R_{MWL} (c,d) as a function of VIS 0.6 μm versus NIR 1.6 μm (a,c), and $\Delta T_{IR10.8-IR12.0}$ versus $\Delta T_{IR8.7-IR10.8}$ (b,d) for Kericho.

As can be seen for the SEVIRI reflectance combination in Figure 5a,c the 0 mm h⁻¹ rainfall scatter throughout the whole range of the satellite signals, with a high concentration of the scatter in the lower-left corner of the plot, where low VIS 0.6 μm reflectance are connected to low NIR 1.6 μm reflectance. On the other hand, the combination of high VIS 0.6 μm versus low NIR 1.6 μm reflectance is generally evident for the occurrence of rainfall. The 0–5 mm h⁻¹ R_{MWL} scatter over a wide range of the satellite signal but with a slight tendency to scatter in the lower right corner of the plot. In some cases, the value combination of the VIS 0.6 μm and NIR 1.6 μm reflectance in this rainfall class were comparable. The rainfall above 5 mm h⁻¹ was generally restricted to the lower right corner of the plot where high VIS 0.6 μm reflectance is connected with low NIR 1.6 μm reflectance.

For the satellite brightness temperature difference (Figure 5b,d) indicative of cloud phase, water ($\Delta T_{IR10.8-IR12.0}$) and ice ($\Delta T_{IR8.7-IR10.8}$), the 0 mm h⁻¹ rainfall also scatter throughout the whole range of the satellite signal, although the values of $\Delta T_{IR10.8-IR12.0}$ were generally higher than those of ($\Delta T_{IR8.7-IR10.8}$). In contrast, the raining satellite signals tend to scatter in a different range of values for $\Delta T_{IR10.8-IR12.0}$ and $\Delta T_{IR8.7-IR10.8}$. Most of the raining satellite signals in the $\Delta T_{IR10.8-IR12.0}$ scatter above 0 K, with a large concentration of the scatter falling within a narrow range (approximately 0 to 1 K) whereas those of $\Delta T_{IR8.7-IR10.8}$, scatter over a large range of values (between -2 and 1.5 K). It can also be seen from the plot that, some coincident values $\Delta T_{IR10.8-IR12.0}$ are larger than those of $\Delta T_{IR8.7-IR10.8}$. Likewise, coincident values of $\Delta T_{IR8.7-IR10.8}$, in some cases, are larger than those of $\Delta T_{IR10.8-IR12.0}$. This was evident for both the rainfall between 0–5 mm h⁻¹ and those above 5 mm h⁻¹ as well from both the R_{RG} and R_{MWL} plots.

The scatter plot of rainfall intensities as a function of the MSG satellite signal during nighttime in May–June 2013 (altogether 218 MSG SEVIRI scenes) is also shown in Figure 6. From the plot, it is clear that the 0 mm h⁻¹ rainfall scatter over the whole range of the satellite signal for all the brightness differences analysed. The raining satellite signals, however, scatter differently for the R_{RG} and R_{MWL} , and in different ranges for all the brightness temperature differences considered.

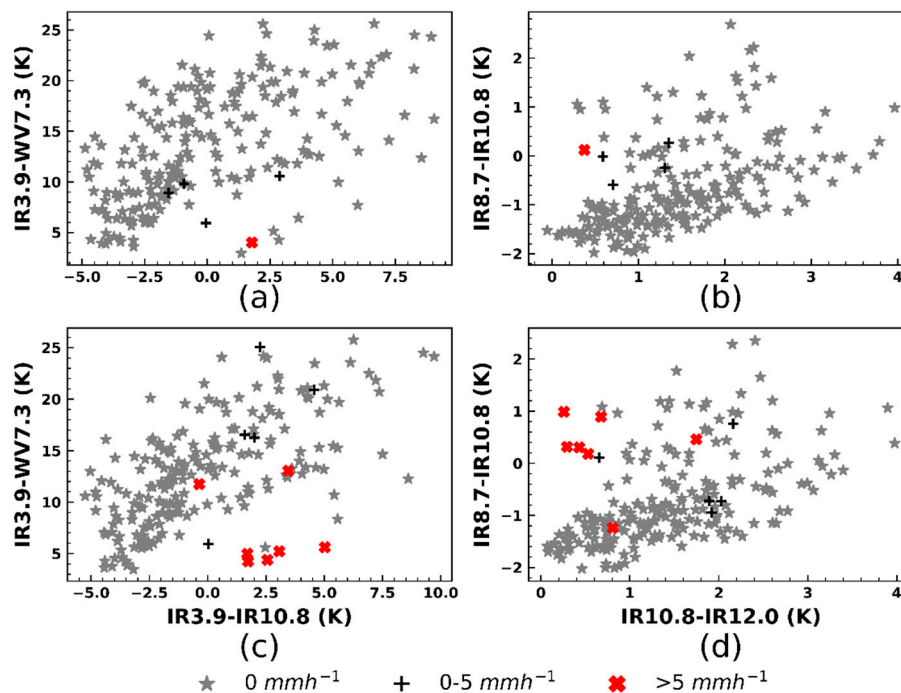


Figure 6. Nighttime R_{RG} (a,b) and R_{MWL} (c,d) as a function of $\Delta T_{IR3.9-IR10.8}$ versus $\Delta T_{IR3.9-WV7.3}$, (a,c) and $\Delta T_{IR10.8-IR12.0}$ versus $\Delta T_{IR8.7-IR10.8}$ (b,d) for Kericho.

For instance, the values of $\Delta T_{IR3.9-WV7.3}$ were larger than those of $\Delta T_{IR3.9-IR10.8}$ (Figure 6a,c). Moreover, the R_{RG} plot (Figure 6a) scatter below 10 K for the $\Delta T_{IR3.9-WV7.3}$ whereas the differences that are shown in the R_{MWL} plot (Figure 6c), in particular, those between 0–5 mm h^{−1}, scatter over a wide range of the satellite signals. On the other hand, the R_{MWL} scatter above 0 K for the $\Delta T_{IR3.9-IR10.8}$ whereas the differences shown in the R_{RG} plot scatter over a wide range (between −5 and 3 K) of the satellite signal.

For the brightness temperature differences in Figure 6 b,d, the $\Delta T_{IR10.8-IR12.0}$ scatter above 0 K with a large concentration of the scatter between 0 and 1 K whereas the $\Delta T_{IR8.7-IR10.8}$ scatter over a comparatively large range of values (between −1.5 and 1 K) of the satellite signal. In addition, some coincident values of $\Delta T_{IR10.8-IR12.0}$ are larger than those of $\Delta T_{IR8.7-IR10.8}$ whereas coincident values of $\Delta T_{IR8.7-IR10.8}$, for some cases, are also larger than those of $\Delta T_{IR10.8-IR12.0}$. This can be observed for both the rainfall between 0–5 mm h^{−1} and those above 5 mm h^{−1} and is evident from the R_{RG} and R_{MWL} plots. Also, these observations were comparable to those found during the daytime analysis.

A scatter plot of rainfall intensity as a function of the MSG satellite signal, analogous to the daytime analysis in Kericho (Figure 5) is presented for Naivasha (Figure 7). Altogether 713 MSG SEVIRI scenes were analysed during the period of May–June 2018. As was also observed in the Kericho analysis (Figure 5), most of the raining satellite signals did not scatter over the whole range of value combinations of satellite reflectance (Figure 7a,c) and brightness temperature difference (Figure 7b,d) and was evident from both the R_{RG} and R_{MWL} plots.

For the satellite reflectance combination, the 0 mm h^{−1} rainfall scatters over the whole range of the satellite signal; and like in the Kericho day time analysis (Figure 5a,c), a large concentration of this scatter was located in the lower-left corner of the plot where VIS 0.6 μ m and NIR 1.6 μ m reflectance were very low. However, in contrast to the daytime analysis in Kericho, the R_{RG} between 0–5 mm h^{−1}, tend to scatter over the whole range of the satellite signals (Figure 7a). Also, for some of the rainfall intensities in this R_{RG} class, the value combination of the VIS 0.6 μ m and NIR 1.6 μ m were comparable. From this plot, it can also be seen that majority of the rainfall above 5 mm h^{−1} scatter in the lower right corner where high VIS 0.6 μ m reflectance were connected to low NIR 1.6 μ m reflectance. Although

some of the R_{RG} above 5 mm h^{-1} do not scatter in the lower right corner, for all these instances the VIS $0.6 \mu\text{m}$ reflectance were higher than those of the NIR $1.6 \mu\text{m}$.

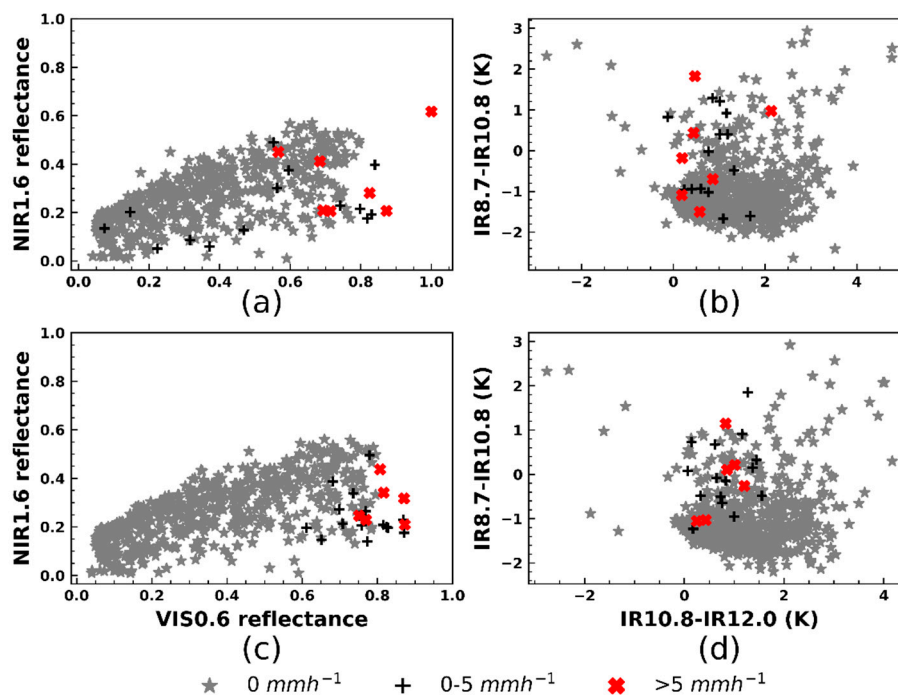


Figure 7. Day time R_{RG} (a,b) and R_{MWL} (c,d) as a function of VIS $0.6 \mu\text{m}$ versus NIR $1.6 \mu\text{m}$ (a,c), and $\Delta T_{IR10.8-IR12.0}$ versus $\Delta T_{IR8.7-IR10.8}$ (b,d) for Naivasha.

As can be seen from the rainfall intensities for the $\Delta T_{IR10.8-IR12.0}$ and $\Delta T_{IR8.7-IR10.8}$ plot (Figure 7b,d), the 0 mm h^{-1} scatter over the whole range of the satellite signal, with generally larger values of $\Delta T_{IR10.8-IR12.0}$ than those of $\Delta T_{IR8.7-IR10.8}$. However, the raining satellite signals scatter over varying ranges of the two brightness temperature differences. For $\Delta T_{IR10.8-IR12.0}$, this range is above 0 K , with the majority of the signals falling between 0 and 1 K . For the $\Delta T_{IR8.7-IR10.8}$, the range is comparatively wider; in particular, the R_{RG} falls between -2 and 2 K . It can also be observed from the plot that, some coincident values of $\Delta T_{IR10.8-IR12.0}$ are larger than those of $\Delta T_{IR8.7-IR10.8}$ and likewise, values of $\Delta T_{IR8.7-IR10.8}$, in some cases are larger than those of $\Delta T_{IR10.8-IR12.0}$. This feature was evident for both the rainfall between $0-5 \text{ mm h}^{-1}$ and those above 5 mm h^{-1} and can as well be seen from the R_{RG} and R_{MWL} plots. Moreover, these observations were also similar to those found in the previous analysis of daytime rainfall intensities and MSG satellite signals in Kericho (Figure 5).

Figure 8 shows rainfall intensities as a function of MSG signals during nighttime in May–June 2018 (altogether 733 MSG SEVIRI scenes) for Naivasha. A clear observation from the figure is that the 0 mm h^{-1} rainfall is scattered over the whole range of values for all the brightness temperature differences presented. Rainfall, however, scatters in a different range of values for the various brightness temperature differences shown.

The $\Delta T_{IR3.9-WV7.3}$ values were generally larger than those of $\Delta T_{IR3.9-IR10.8}$ (Figure 8a,c), with rainfall scattering below 15 K for the $\Delta T_{IR3.9-WV7.3}$ and between -5 and 5 K for $\Delta T_{IR3.9-IR10.8}$. Moreover, most of the R_{RG} between $0-5 \text{ mm h}^{-1}$ scatter over a larger $\Delta T_{IR3.9-WV7.3}$ than those above 5 mm h^{-1} (Figure 8a), whereas in the R_{MWL} plot (Figure 8c), both rainfall intensity classes tend to scatter over a wide range.

From the rainfall intensity scatter plot for $\Delta T_{IR10.8-IR12.0}$ and $\Delta T_{IR8.7-IR10.8}$ (Figure 8b,d), it can also be observed that most of the rainfall scatter above 0 K for the $\Delta T_{IR10.8-IR12.0}$, and between -2 and 2 K for the $\Delta T_{IR8.7-IR10.8}$. It is also clear from this plot that, the rainfall between $0-5 \text{ mm h}^{-1}$ scatter differently from those above 5 mm h^{-1} . In particular, the R_{RG} between $0-5 \text{ mm h}^{-1}$ scatters over a wide

range of value combinations of $\Delta T_{\text{IR}10.8-\text{IR}12.0}$ and $\Delta T_{\text{IR}8.7-\text{IR}10.8}$. By contrast, the rainfall intensities above 5 mm h^{-1} are grouped in a narrow range of value combinations of the brightness temperature differences (Figure 8b). This feature can also be observed in the R_{MWL} (Figure 8d), although here, the rainfall above 5 mm h^{-1} showed a slight tendency to scatter over a wide range of values.

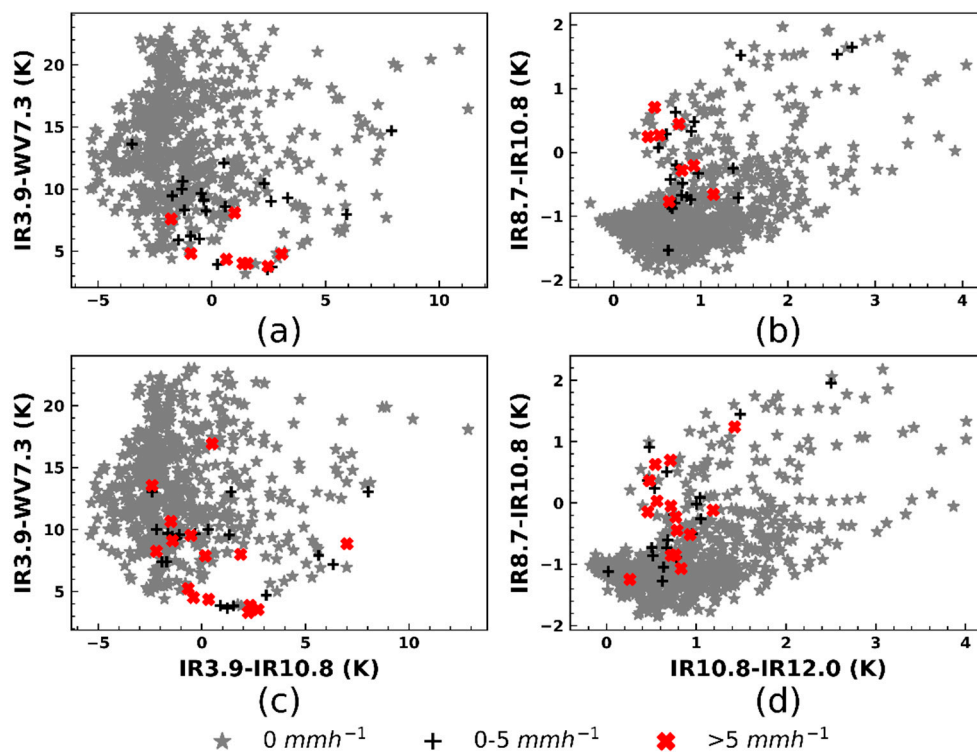


Figure 8. Nighttime R_{RG} (a,b) and R_{MWL} (c,d) as a function of $\Delta T_{\text{IR}3.9-\text{IR}10.8}$ versus $\Delta T_{\text{IR}3.9-\text{WV}7.3}$, (a,c) and $\Delta T_{\text{IR}10.8-\text{IR}12.0}$ versus $\Delta T_{\text{IR}8.7-\text{IR}10.8}$ (b,d) for Naivasha.

(ii) Inferences from analyzing rainfall estimates with MSG satellite data

Overall, it can be stated based on the observations in Figures 5 and 7 that, most of the rain cases (i.e., $0-5 \text{ mm h}^{-1}$ and above 5 mm h^{-1}) defined by R_{RG} and R_{MWL} during day time were covered by optically thick clouds that were characterized by high VIS $0.6 \mu\text{m}$ and low NIR $1.6 \mu\text{m}$ reflectance, and with different ranges of $\Delta T_{\text{IR}10.8-\text{IR}12.0}$ and $\Delta T_{\text{IR}8.7-\text{IR}10.8}$. The high VIS $0.6 \mu\text{m}$ and low NIR $1.6 \mu\text{m}$ reflectance is an indication of the cloud's large CWP and high rainfall probabilities and intensities [39]. Notice that the $\Delta T_{\text{IR}10.8-\text{IR}12.0}$ (between 0 and 1 K) and $\Delta T_{\text{IR}8.7-\text{IR}10.8}$ (between -2 and 2 K) ranges found in this study were also indicative of medium (i.e., low optical thickness with large particle sizes and high optical thickness with small particle sizes) to large (i.e., high optical thickness with large particle sizes) CWP with high rainfall probabilities and intensities according to radiative transfer calculation by [38]. Further, the value ranges of $\Delta T_{\text{IR}10.8-\text{IR}12.0}$ and $\Delta T_{\text{IR}8.7-\text{IR}10.8}$ are characteristic of optically thick cumulous-type clouds with ice at the top, based on cloud classification presented by [74,96]. In contrast, most of the no rain cases (i.e., 0 mm h^{-1}) correspond to non-precipitating thin and thick cirrus clouds and N-type clouds (edges of optically thick clouds, optically thinner cumulous clouds, or low-level cumulous cloud overlaid by thin cirrus clouds) [74,85].

During nighttime (Figures 6 and 8), most of the rain cases (i.e., $0-5 \text{ mm h}^{-1}$ and above 5 mm h^{-1}) defined by R_{RG} and R_{MWL} were covered by optically thick clouds with medium $\Delta T_{\text{IR}3.9-\text{IR}10.8}$ (between -5 and 5 K) and $\Delta T_{\text{IR}3.9-\text{WV}7.3}$ (between 5 and 10 K). [38] showed that medium $\Delta T_{\text{IR}3.9-\text{IR}10.8}$ values are linked to large CWP with high rainfall probabilities and intensities. High and small $\Delta T_{\text{IR}3.9-\text{IR}10.8}$ is, however, indicative of medium CWP with low rainfall probabilities and intensities. The results for

$\Delta T_{IR3.9-WV7.3}$ show comparable characteristics to $\Delta T_{IR3.9-IR10.8}$ but with generally higher $\Delta T_{IR3.9-WV7.3}$ than $\Delta T_{IR3.9-IR10.8}$ differences. The higher $\Delta T_{IR3.9-WV7.3}$ differences than $\Delta T_{IR3.9-IR10.8}$ can be explained by the diminishing effect of the water vapour absorption and emission in the mid-to-low tropospheric levels on the brightness temperature in WV7.3 μm channel [54]. For the $\Delta T_{IR8.7-IR10.8}$ versus $\Delta T_{IR10.8-IR12.0}$ difference, the observations made for both rain and no rain cases were comparable to those found during the daytime analysis.

The results are consistent with the conceptual model introduced in Section 3.3.1 that clouds with high optical thickness and large particle sizes, indicative of large CWP (with the existence of ice or water hydrometeors at the top) have a high probability of producing rainfall.

Finally, an inspection of Figures 5–8 raises the possibility of distinguishing rain and no rain cases based on a combination of parameters: VIS 0.6 μm , NIR 1.6 μm , $\Delta T_{IR10.8-IR12.0}$ and $\Delta T_{IR8.7-IR10.8}$ (for during day time), and $\Delta T_{IR3.9-WV7.3}$, $\Delta T_{IR3.9-IR10.8}$, $\Delta T_{IR10.8-IR12.0}$ and $\Delta T_{IR8.7-IR10.8}$ (for during nighttime). This can be achieved using statistical machine learning or parametric (threshold) techniques, e.g., [72,74]. Here, we empirically defined parametric thresholds based on descriptive statistics of the SEVIRI satellite signals for the rain cases, for rainfall detection.

4.1.3. Rainfall Detection with MSG SEVIRI Data

The different combination of MSG channels that were jointly analysed with rainfall data in the previous section was used to test rain detection on individual MWL. In this section, the results of detecting rain on MWL using MSG SEVIRI satellite signals are presented.

In Table A1, the calculated descriptive statistics of SEVIRI satellite signals for each of the R_{MWL} class are shown per each study location for both day and nighttime. A summary of the data used for calculating these statistical values are shown in Table 5, and the data were analysed in Figures 5–8 in the previous section. What is clear from Table A1 is the low and high standard deviation values of the reflectance and brightness temperature differences, respectively. When the standard deviation is interpreted together with the mean, mode, and median values, it becomes evident that the satellite reflectance tends to spread close to their mean. In contrast, the brightness temperature differences spread over a large range of values. Moreover, there were large differences in the statistical values between raining and non-raining satellite signals. However, the differences in statistical values between 0–5 mm h^{-1} and above 5 mm h^{-1} rainfall classes were rather low.

Based on the descriptive statistics in Table A1, reflectance threshold and brightness temperature difference range (Table 6) were derived that were used to compute the elements a , b , c , and d in Equations (8)–(15) for rainfall detection. Since the satellite signals of 0–5 mm h^{-1} and above 5 mm h^{-1} rainfall classes were not statistically different, separate threshold and brightness temperature difference range for the two-classes was not necessary. Thus, a single threshold and brightness temperature difference range were defined separately for day and nighttime, and the two study locations. The reflectance thresholds: $\text{Vis}_{\text{thres}}$ and $\text{Nir}_{\text{thres}}$ (Table 6) were derived from the median and mean statistical values respectively, whereas the brightness temperature difference range was derived from a combination of minimum, maximum, mean and mode values, depending on the channel difference. The results in Table 6 show that the reflectance thresholds were comparable (during daytime). In contrast, the brightness temperature difference ranges (during day and nighttime) varied across the two study locations.

Table 6. Reflectance threshold and brightness temperature range used for rain detection.

Study Location	Time	Vis _{thres}	Nir _{thres}	$\Delta T_{IR8.7-IR10.8}$ Range K	$\Delta T_{IR10.8-IR12.0}$ Range K
Kericho	Day	>0.70	<0.43	−1.0–1.42	−1.0–1.0
Naivasha		>0.70	<0.50	−1.10–1.15	0.0–1.2
		$\Delta T_{IR3.9-IR10.8}$ range K	$\Delta T_{IR3.9-WV7.3}$ range K	$\Delta T_{IR8.7-IR10.8}$ range K	$\Delta T_{IR10.8-IR12.0}$ range K
Kericho	Night	2.0–5.0	4.0–12.0	−0.01–1.0	0.26–1.9
Naivasha		−3.0–1.0	3.0–15.0	−1.0–2.0	0.0–1.0

Table 7 summarises the verification scores of the satellite-based rain detection on MWL for Kericho and Naivasha, during the day and nighttime. The scores are based on MWL and satellite data from the two study locations, that are independent of those used in the previous analysis in Section 4.1.2. The numbers in Table 7 (first column) are used to represent the MWL name and were derived from the link identification supplied by the telecommunication provider. The scores were computed across the evaluation period, and for MWL, from which more than five R_{MWL} were retrieved during day or nighttime.

The results, as shown in Table 7, were effective in identifying periods of no rain. As can be seen from the percentage of correct negatives, more than 95% of no rain on individual MWL was correctly identified by the test on the satellite signals as non-raining. However, the rain detection skill varied between the day and nighttime, as can be seen from the hit percentage.

In Kericho, the day time detection performed better than nighttime detection. For most of the MWL, between 58.1% and 78.6% of the R_{MWL} were successfully detected, and between 21.4% and 42.9% were incorrectly identified as non-raining. For the nighttime, between 25% and 50% of success was achieved, and between 50% and 75% of the R_{MWL} , was incorrectly detected as non-raining. The percentage of false alarms, FAR and POFD were generally higher in the daytime than the nighttime. Nonetheless, the good performance of the daytime detection over the nighttime was supported by the POD, CSI and HSS scores. The range of values computed for the daytime were between: 0.57 and 0.79 (POD); 0.4 and 0.61 (CSI) and 0.55 and 0.75 (HSS), whereas for the nighttime, values ranging between: 0.25 and 0.5; 0.24 and 0.444 and 0.4 and 0.6 were computed for POD, CSI and HSS, respectively. Altogether, the accuracy scores were high for both the day and nighttime test. This can be attributed to the effectiveness of the method in detecting no rain on individual MWL.

Similarly, the daytime detection results in Naivasha were comparatively better than those of nighttime. For daytime, it succeeded in detecting between 57.1% and 62.5% of the R_{MWL} , and between 35% to 42.9% were erroneously detected as non-raining. However, for the nighttime, between 30% and 91.7% of success was achieved, with 8.3% to 70% of the R_{MWL} , erroneously identified as non-raining. The percentage of false alarms, FAR and POFD for the daytime were lower than the nighttime. The scores of POD, CSI, and HSS further support the good performance of the day time over the nighttime. For the daytime: POD range between 0.57 and 0.65; CSI range between 0.44 and 0.62; and HSS range between 0.61 and 0.76. For the nighttime, values ranging between 0.3 and 0.92; 0.14 and 0.58 and 0.23 and 0.73 were computed for POD, CSI, and HSS respectively. Regarding the overall accuracy for the day and nighttime, the previous comment for the Kericho case is also valid.

Table 7. Computed performance verification scores of rain detection using MWL and MSG data.

MWL Name?	¹ R_{MWL} (mm)	Hits %	Miss %	False Alarms %	Correct Negatives %	POD	FAR	POFD	ACC	CSI	HSS
Perfect score		-	-	-	-	1	0	0	1	1	1
Kericho MWL											
					Day time						
13471368	311.32	58.1	41.9	29	96.4	0.58	0.33	0.04	0.92	0.45	0.58
13671368	230.87	78.6	21.4	28.6	98.4	0.79	0.27	0.02	0.97	0.61	0.75
30941368	331.15	57.1	42.9	17.9	98.4	0.57	0.24	0.02	0.94	0.49	0.62
30953094	83.53	66.7	33.3	66.7	98.1	0.67	0.50	0.03	0.96	0.40	0.55
34051368	437.98	65	35	50	96.3	0.65	0.44	0.04	0.94	0.43	0.57
					Nighttime						
13471368	124.62	50	50	30	98.5	0.50	0.38	0.02	0.96	0.39	0.5
13671368	138.43	25	75	6.2	99.5	0.25	0.2	0.01	0.94	0.24	0.4
30941368	112.65	41.7	58.3	8.3	99.5	0.42	0.18	0.01	0.96	0.39	0.5
30953094	68.72	50	50	12.5	99.5	0.50	0.2	0.01	0.98	0.44	0.6
Naivasha MWL											
					Day time						
13201328	77.0	65	35	5	99.8	0.65	0.07	0.002	0.99	0.62	0.76
34101372	203.73	61.5	38.5	15.4	99.6	0.62	0.20	0.004	0.99	0.53	0.69
13723379	201.47	57.1	42.9	28.6	99.6	0.57	0.33	0.004	0.99	0.44	0.61
1372	187.10	62.5	37.5	25	99.6	0.63	0.29	0.004	0.99	0.50	0.66
13201327	80.22	60	40	5	99.8	0.6	0.08	0.02	0.98	0.57	0.72
13071372	232.91	61.5	38.5	15.4	99.6	0.62	0.20	0.004	0.99	0.53	0.69
					Nighttime						
13201328	42.10	91.7	8.3	58.3	98.9	0.92	0.39	0.011	0.99	0.58	0.73
13723365	169.10	57.1	42.9	78.6	97.7	0.57	0.58	0.023	0.97	0.32	0.47
13201327	21.57	30	70	120	98.2	0.3	0.8	0.018	0.97	0.14	0.23
13263035	46.46	60	40	100	98.9	0.6	0.63	0.011	0.99	0.3	0.46
13263302	55.34	45.5	54.5	54.5	98.7	0.46	0.55	0.013	0.97	0.29	0.44

¹ Accumulated R_{MWL} for each MWL computed across the evaluation period.

4.2. Discussion

4.2.1. Accuracy of the MWL Rainfall Estimates

Two MWL of the same frequency (15 GHz) but different lengths: 3.7 and 10 km, and from different study locations: Kericho and Naivasha were used to estimate R_{MWL} . The results were then compared, at different evaluation timestamps, with R_{RG} derived from rain gauges. Overall, the results demonstrate the potential and capacity of MWL networks to provide rainfall data in areas where ground monitoring systems are lacking or insufficient. The overall accuracy of the R_{MWL} derived from the two MWL can be described as good. Despite the high values of CV observed, the low RB and RMSE values show that reliable rainfall information can be derived from MWL networks. The hourly r^2 values were about 0.60, for both MWL and more specifically for the Naivasha link, and the values for all evaluation timestamps were above 0.5, which can be described as convincing considering these values were achieved at fine resolution.

The discrepancies found between R_{MWL} and R_{RG} are expected when comparing rainfall data from two sensors with differences in their nature of measurement. The R_{MWL} were retrieved from the mean RSL data that were derived every 15 min from instantaneous RSL measurements. On the other hand, the R_{RG} was computed from rain gauges that recorded rainfall accumulations every minute. Also, the differences between R_{MWL} and R_{RG} could be explained in part by uncertainties in the R_{MWL} rainfall estimation approach [97–99]. Additionally, the discrepancies could be due to the spatial variability of rainfall [100].

4.2.2. The Analysis of R_{MWL} with MSG SEVIRI Data

R_{MWL} from the two links presented above were jointly analysed with satellite signals from MSG SEVIRI solar and thermal infrared channels. Both data were temporarily aggregated, and the satellite data were spatially aggregated to reduce the effect of potential temporal and spatial mismatch between the rainfall and satellite data in our analysis. The premise for analyzing the MWL rainfall with the SEVIRI data is that raining clouds that attenuate individual MWL can be detected based on their cloud top properties, using the satellite data. Therefore, a conceptual model was defined for detecting rainfall based on the assumption that clouds with high cloud top optical thickness and large particle sizes (with the existence of ice or water hydrometeors) have high rainfall probabilities and intensities. During day time, the model infers cloud top optical thickness and particle sizes from SEVIRI solar channels: VIS 0.6 μm and NIR 1.6 μm , respectively, whereas the brightness temperature difference between IR 8.7 μm and 10.8 μm ($\Delta T_{IR8.7-IR10.8}$) and that between IR 10.8 μm and 12.0 μm ($\Delta T_{IR10.8-IR12.0}$), supplied additional information on cloud phase namely: ice and water, respectively. During the nighttime, the brightness temperature differences: $\Delta T_{IR3.9-IR10.8}$, $\Delta T_{IR3.9-WV7.3}$, $\Delta T_{IR8.7-IR10.8}$, and $\Delta T_{IR10.8-IR12.0}$ were used to infer similar information about the cloud top properties.

When R_{MWL} was considered as a function of cloud optical thickness (VIS 0.6 μm reflectance) and particle sizes (NIR 1.6 μm reflectance) during daytime, the raining satellite signals had high values of VIS 0.6 μm and low values of NIR 1.6 μm reflectance. On the other hand, R_{MWL} as a function of $\Delta T_{IR8.7-IR10.8}$ and $\Delta T_{IR10.8-IR12.0}$, showed that the raining satellite signals grouped in a different range of values of the two brightness temperature differences. $\Delta T_{IR8.7-IR10.8}$, indicative of ice clouds, covered a large range of values while $\Delta T_{IR10.8-IR12.0}$, indicative of water clouds, a narrow range. The nighttime analysis of R_{MWL} as a function of $\Delta T_{IR3.9-WV7.3}$ and $\Delta T_{IR3.9-IR10.8}$ also showed that the raining satellite signals spread over a wide range of value combination of $\Delta T_{IR3.9-WV7.3}$ and $\Delta T_{IR3.9-IR10.8}$. The differences of $\Delta T_{IR3.9-WV7.3}$ were, however, mostly higher than those of $\Delta T_{IR3.9-IR10.8}$. For the analysis R_{MWL} as a function of $\Delta T_{IR8.7-IR10.8}$, and $\Delta T_{IR10.8-IR12.0}$, the range of brightness temperature differences in the raining satellite signals were comparable to those found in the daytime analysis.

The above results corroborate the proposed conceptual model that clouds with high optical thickness and large particle sizes (with ice or water particles at the top) have high rainfall probability

and show the possibility for an area-wide rainfall detection based on the combination of the different MSG satellite signals for both day and night.

A test for detecting rainfall on individual MWL using the different kinds of MSG SEVIRI channels analysed in this study was also presented. The results indicate an appreciable capability of the satellite data to detect rainfall intensities on individual MWL. The verification scores showed that the test performed better during daytime and comparable across the two study locations. This could be due to the higher and reliable information content on CWP and rainfall, that is available in the VIS 0.6 μm and NIR 1.6 μm reflectance pair, compared to channel differences used during nighttime [80]. As was also shown in the results, a strong relationship can be found between VIS 0.6 μm and NIR 1.6 μm reflectance (Figure 5a,c and Figure 7a,c) and R_{MWL} during the daytime. Moreover, descriptive statistical values from the analysis of R_{MWL} and satellite data indicate that the daytime satellite reflectance was statistically different between the rain and non-raining satellite signals. This might explain the high rain detection with good CSI and HSS scores based on the daytime test. The statistical values derived from the nighttime data were rather often comparable between rain and non-raining satellite signals and could explain its high false detection with comparatively weak CSI and HSS scores.

The good performance of the test suggests that the MWL and MSG data have the potential for area-wide rainfall studies. A possible implication is that the MWL and MSG data could be potential input to optical satellite-based models for rainfall detection and estimation. In this context, data fusion [101,102] and statistical machine learning offer techniques to explore relationships (linear and non-linear) between multiple large input variables. Further, current developments in parallel computing with machine learning have increased the training and predicting speeds of these learning algorithms and can make the automatization and improvement of the method in real-time feasible [103,104]. Also, for MWL based rainfall studies in areas lacking in-situ data, the results suggest that the satellite-based rain information may be a useful tool for wet/dry classification of the MWL signal. Therefore, future research involving analysis with large datasets would also focus on investigating the MWL and satellite data for such an application.

Uncertainties that were found in the analysis of R_{MWL} with MSG satellite data could be due to measurement differences between the satellite and MWL. The satellite signal is acquired instantaneously over an area, while the R_{MWL} is acquired from MWL every 15 min, and is representative along the link transmission path. It is therefore not surprising that the satellite signal might not correspond with the rainfall intensities. Furthermore, the spatiotemporal aggregation employed to retrieve the most effective satellite signal from the satellite data is perhaps not enough to compensate for measurement differences inherent of the two sensors. Additionally, horizontal wind drift within or outside raining clouds will have a strong influence on falling hydrometeors of light rainfall. It could explain in part, the high uncertainty that was observed for the 0–5 mm h^{-1} rainfall intensity class. In case of deep convective cores with anvil cloud areas, the retrieval of the satellite signal of high rainfall intensities clouds might be biased towards anvil cloud areas, which have characteristics of light rainfall intensities. This could explain why some rainfall intensities above 5 mm h^{-1} (e.g., Figure 5c) did not correspond with the satellite signals. Moreover, in the case of multilayered clouds [105], with cloud properties differing between layers, the satellite signals may not correlate with the ground rainfall [106].

To this end, the ability to distinguish different raining cloud types, e.g., convective/stratiform and track their footprints surrounding the individual MWL will provide valuable information relevant for retrieving and linking the MSG satellite signals to the MWL rainfall. The identification of different cloud types and tracking their location around the MWL should reduce the spatial aggregation problems (Section 3.3.2) and the resulting uncertainties between MWL rainfall and the MSG satellite signals. In this context, the promising results demonstrated by [68,80,107,108] for raining cloud classification and [109,110] for tracking raining clouds accentuate the potential of a more accurate MWL and satellite-based raining cloud detection. Thus, future studies which consider these concepts will be undertaken.

5. Conclusions

This study investigated the combination of MWL rainfall estimates with MSG SEVIRI satellite data for rainfall detection using observations from two areas in Kenya: Kericho and Naivasha. The approach involves: (i) an evaluation of the MWL rainfall estimates using an experimental setup consisting of two MWL (of varying lengths) and several rain gauge measurements as ground truth; (ii) next, the MWL rainfall estimates were analysed as a function of the MSG SEVIRI satellite signals. The satellite signals were used to infer information on cloud top properties by means of a conceptual model that, clouds with high cloud top optical thickness and large particle size (with ice or water hydrometeors) are linked to high rainfall probabilities and intensities; (iii) finally, the information content gained from analyzing the MWL rainfall with MSG SEVIRI satellites signals, was then used for detecting rainfall on individual MWL.

The results show that the MWL can estimate rainfall intensities with reliable accuracies when compared with rain gauges. However, limitations, such as inherent measurement differences between the MWL and the gauge, remain a challenge and affect rainfall retrieval accuracies.

Analysing the MWL rainfall estimates as a function of the MSG satellite signals, revealed characteristics of the raining satellite signals that corroborates with the conceptual model for detecting raining clouds. During the daytime, high VIS $0.6\ \mu\text{m}$ and low NIR $1.6\ \mu\text{m}$ reflectance (indicative of high optical thickness and large particle sizes and thus large CWP) were often consistent with MWL rainfall between $0\text{--}5\ \text{mm h}^{-1}$ and above $5\ \text{mm h}^{-1}$. These raining satellite signals also differed from the non-raining satellite signals (satellite signals indicative of $0\ \text{mm h}^{-1}$) and were comparable across the two study locations. For nighttime, MWL rainfall between 0 and $5\ \text{mm h}^{-1}$ and above $5\ \text{mm h}^{-1}$ was characterized by $\Delta T_{\text{IR}3.9\text{--IR}10.8}$ and $\Delta T_{\text{IR}3.9\text{--WV}7.3}$ brightness temperature ranges, indicative of medium to large CWP. Nonetheless, the ranges varied between the two study areas and were not different between rain and non-raining satellite signals. Additionally, day and night temperature ranges of $\Delta T_{\text{IR}8.7\text{--IR}10.8}$ and $\Delta T_{\text{IR}10.8\text{--IR}12.0}$ for the MWL rainfall between 0 and $5\ \text{mm h}^{-1}$ and above $5\ \text{mm h}^{-1}$ suggests that most of the rain cases were from optically thick cumulous-type clouds.

The analysis also produced descriptive statistics: minimum, maximum, mean, mode, median and standard deviation of the satellite signal, from which threshold and brightness temperature difference range were derived for testing the potential of the combining information from the different satellite signals to detect rainfall on MWL. Overall, the verification scores indicate a considerable capability of the satellite data to detect rainfall on MWL, particularly during the daytime.

The findings of this study should be interpreted while considering the potential limitations of the study. The assumed relationship between MWL rainfall and MSG SEVIRI satellite signals (for inferring cloud optical and microphysical properties) was confirmed using a limited dataset and of local origin. Thus, the descriptive statistics of the rain and non-raining satellite and the corresponding parameters (i.e., the thresholds and brightness temperature difference ranges) should be considered restricted to the study locations. Nonetheless, the approach is applicable to other areas to retrieve representative thresholds using sufficient dataset. Moreover, to allow for the operational and large-scale application of MWL and MSG data for rainfall studies based on the findings of this study, further research involving large datasets are necessary to support the observed relation between MWL rainfall and MSG based cloud top properties. In this regard, the dataset should be enlarged in both space and time. A larger time series of MWL and MSG data pairs that is retrieved from a spatially dense MWL network should compute more representative descriptive statistics and parameter estimates while improving the retrieval technique [111]. Also, data fusion and machine learning techniques offer possibilities for exploring relationships between large numbers of input variables from different sensors. These learning algorithms provide efficient alternatives and may be suitable to overcome limitations of parametric approaches (as demonstrated in this study), while potentially automating the retrieval approach [103,112].

Altogether, it can be stated based on the findings of this study that, the combination the MWL rainfall and MSG SEVIRI data have the potential for area-wide rainfall detection at a high temporal

resolution. This is especially significant for areas lacking in-situ monitoring systems but having good MWL coverage established (and maintained) over the last decade, and being still further developed. Using both in-situ and MW-link data will potentially enhance the density of the observation network to monitor rainfall on the ground, and with high temporal resolution remote sensing derived information, as acquired by geostationary satellites, better temporal and spatial extrapolation will be possible.

Author Contributions: Conceptualization of the study: B.Z.S., J.C.B.H., B.H.P.M., and K.K.K.; fieldwork and experimental design: J.C.B.H. and K.K.K.; methodology (MWL data analysis): K.K.K., N.D., and H.O.G.; methodology (satellite data acquisition and analysis): K.K.K., B.H.P.M., and J.C.B.H.; manuscript preparation and editing: K.K.K. with help from N.D., B.H.P.M., J.C.B.H., H.O.G., and B.Z.S. All authors have read and agreed to the published version of the manuscript.

Funding: This research received no external funding except for the support provided by the Consultative Group on International Agricultural Research (CGIAR) Research Program on Climate Change, Agriculture and Food Security (CCAFS) during the 2013 field campaigns in Kericho.

Acknowledgments: The authors express their gratitude to Safaricom for providing the MWL RSL data, and to TAHMO for assessing their station (gauge) data. An appreciation is extended to James Finlays Kenya and the Kericho Tea Hotel for allowing us to carry our experimental measurements on their premises in Kericho. The authors would also like to credit VP Group in Naivasha for their cooperation during the Naivasha fieldwork, Paul Ruoya and the farmers in the Naivasha catchment who allowed us to carry out field measurements on their farm. Some of the experimental work for this study was also carried out with support from the Consultative Group on International Agricultural Research (CGIAR) Research Program on Climate Change, Agriculture and Food Security (CCAFS).

Conflicts of Interest: The authors declare no conflict of interest.

Appendix A

Table A1. Descriptive statistics of SEVIRI satellite signals for each rainfall intensity class and study location.

MSG Signal	R_{MWL} (mm h ⁻¹)	Min	Max	Mean	Mode	Median	SD
Kericho							
Day time							
VIS 0.6 μ m	0	0.073	0.886	0.417	0.3	0.38	0.215
	0–5	0.562	0.972	0.74	0.8	0.77	0.15
	>5	0.374	1	0.726	0.7	0.726	0.148
NIR 1.6 μ m	0	0.036	0.858	0.337	0.3	0.32	0.132
	0–5	0.31	0.608	0.433	0.3	0.384	0.137
	>5	0.178	0.536	0.304	0.3	0.296	0.09
$\Delta T_{IR8.7-IR10.8}$	0	−2.357	2.177	−0.613	−1	−0.756	0.88
	0–5	−1.826	1.417	−0.453	−	−0.57	1.10
	>5	−1.721	1.42	−0.137	−0.9	−0.354	0.915
$\Delta T_{IR10.8-IR12.0}$	0	−0.55	4.336	1.711	2.3	1.736	0.98
	0–5	−0.215	2.366	0.737	0.9	0.617	0.914
	>5	−1.836	2.064	0.469	0.8	0.561	0.749
Nighttime							
$\Delta T_{IR3.9-IR10.8}$	0	−5.252	9.709	−0.204	−1.6	−1.166	3.194
	0–5	0.033	4.57	2.087	−	1.998	1.633
	>5	−0.366	5.026	2.454	1.7	2.563	1.686
$\Delta T_{IR3.9-WV7.3}$	0	3.466	25.765	12.884	13.2	12.64	5.122
	0–5	5.933	25.068	16.938	−	16.537	7.134
	>5	4.234	13.046	7.033	−	5.226	3.711
$\Delta T_{IR8.7-IR10.8}$	0	−2.024	2.354	−0.702	−1.1	−0.959	0.894
	0–5	−0.944	0.76	−0.306	−0.7	−0.724	0.72
	>5	−1.242	0.988	0.272	0.3	0.318	0.734
$\Delta T_{IR10.8-IR12.0}$	0	0.072	3.976	1.449	1.5	1.365	0.808
	0–5	0.655	2.162	1.732	1.9	1.918	0.611
	>5	0.258	1.748	0.678	0.3	0.532	0.511

Table A1. Cont.

MSG Signal	R_{MWL} (mm h ⁻¹)	Min	Max	Mean	Mode	Median	SD
Naivasha							
Day time							
VIS 0.6 μ m	0	0.04	0.795	0.338	0.1	0.314	0.221
	0–5	0.611	0.871	0.758	0.8	0.764	0.075
	>5	0.751	0.873	0.815	0.8	0.812	0.05
NIR 1.6 μ m	0	0.01	0.561	0.256	0.2	0.239	0.124
	0–5	0.14	0.495	0.244	0.2	0.21	0.093
	>5	0.209	0.437	0.296	0.2	0.281	0.086
$\Delta T_{IR8.7-IR10.8}$	0	−2.199	2.923	−0.973	−1.2	−1.184	0.775
	0–5	−1.232	1.85	−0.066	−0.5	0.114	0.834
	>5	−1.054	1.146	−0.146	-	−0.077	0.835
$\Delta T_{IR10.8-IR12.0}$	0	−2.76	4.17	1.31	1.8	1.282	0.859
	0–5	0.073	1.556	0.786	0.1	0.748	0.497
	>5	0.249	1.202	0.763	-	0.843	0.359
Nighttime							
$\Delta T_{IR3.9-IR10.8}$	0	−5.37	12.848	−1.162	−2.5	−1.972	2.436
	0–5	−2.404	8.041	0.844	-	0.315	3.036
	>5	−2.4	6.999	0.537	-	0.166	2.42
$\Delta T_{IR3.9-WV7.3}$	0	3.834	22.985	13.495	11.7	13.33	4.015
	0–5	3.648	13.04	8.537	13	9.44	2.967
	>5	3.317	16.932	7.845	-	7.994	3.902
$\Delta T_{IR8.7-IR10.8}$	0	−1.851	2.175	−0.84	−1.2	−1.071	0.709
	0–5	−1.277	1.953	−0.144	−0.9	−0.258	0.884
	>5	−1.246	1.239	−0.171	−0.1	−0.145	0.697
$\Delta T_{IR10.8-IR12.0}$	0	−0.181	4.008	0.945	0.9	0.851	0.715
	0–5	0.017	2.504	0.809	0.5	0.674	0.514
	>5	0.258	1.426	0.742	0.8	0.72	0.289

Continuation of Table A1. Note: (-) imply no value was computed for that particular class, Min is Minimum, Max is Maximum, and SD is the standard deviation.

References

- Hong, Y.; Adler, R.F.; Negri, A.; Huffman, G.J. Flood and landslide applications of near real-time satellite rainfall products. *Nat. Hazards* **2007**, *43*, 285–294. [\[CrossRef\]](#)
- Levizzani, V.; Bauer, P.; Turk, F.J. *Measuring Precipitation from Space: EURAINSAT and the Future*; Springer: Dordrecht, The Netherlands, 2007; Volume 28, p. 722.
- Cristiano, E.; ten Veldhuis, M.-C.; van de Giesen, N. Spatial and temporal variability of rainfall and their effects on hydrological response in urban areas—A review. *Hydrol. Earth Syst. Sci.* **2017**, *21*, 3859–3878. [\[CrossRef\]](#)
- Michaelides, S.; Levizzani, V.; Anagnostou, E.; Bauer, P.; Kasparis, T.; Lane, J.E. Precipitation: Measurement, remote sensing, climatology and modeling. *Atmos. Res.* **2009**, *94*, 512–533. [\[CrossRef\]](#)
- Rios, G.M.F.; Aart, O.; Hidde, L.; Marc, B.; Remko, U. Rainfall Field Estimation Using Simulated Microwave Link Information. Master's Thesis, Faculty of Geosciences, Utrecht University, Utrecht, The Netherlands, 2012.
- Villarini, G.; Mandapaka, P.V.; Krajewski, W.F.; Moore, R.J. Rainfall and sampling uncertainties: A rain gauge perspective. *J. Geophys. Res. Atmos.* **2008**, *113*, 1–12. [\[CrossRef\]](#)
- Tang, G.Q.; Ma, Y.Z.; Long, D.; Zhong, L.Z.; Hong, Y. Evaluation of GPM Day-1 IMERG and TMPA Version-7 legacy products over Mainland China at multiple spatiotemporal scales. *J. Hydrol.* **2016**, *533*, 152–167. [\[CrossRef\]](#)
- Barthès, L.; Mallet, C. Rainfall measurement from the opportunistic use of an Earth-space link in the Ku band. *Atmos. Meas. Tech.* **2013**, *6*, 2181–2193. [\[CrossRef\]](#)
- Upton, G.J.G.; Holt, A.R.; Cummings, R.J.; Rahimi, A.R.; Goddard, J.W.F. Microwave Links: The Future For Urban Rainfall Measurement? *Atmos. Res.* **2005**, *77*, 300–312. [\[CrossRef\]](#)

10. Dinku, T.; Chidzambwa, S.; Ceccato, P.; Connor, S.J.; Ropelewski, C.F. Validation of satellite rainfall products over East Africa's complex topography. *Int. J. Remote Sens.* **2008**, *29*, 4097–4110. [[CrossRef](#)]
11. Kidd, C.; Becker, A.; Huffman, G.J.; Muller, C.L.; Joe, P.; Skofronick-Jackson, G.; Kirschbaum, D.B. So, how much of the Earth's surface is covered by rain gauges? *Bull. Am. Meteorol. Soc.* **2017**, *98*, 69–78. [[CrossRef](#)]
12. Lengfeld, K.; Clemens, M.; Münster, H.; Ament, F. Performance of high-resolution X-band weather radar networks - The PATTERN example. *Atmos. Meas. Tech.* **2014**, *7*, 4151–4166. [[CrossRef](#)]
13. Uijlenhoet, R.; Berne, A. Stochastic simulation experiment to assess radar rainfall retrieval uncertainties associated with attenuation and its correction. *Hydrol. Earth Syst. Sci.* **2008**, *12*, 587–601. [[CrossRef](#)]
14. Villarini, G.; Krajewski, W.F. Review of the Different Sources of Uncertainty in Single Polarization Radar-Based Estimates of Rainfall. *Surv. Geophys.* **2010**, *31*, 107–129. [[CrossRef](#)]
15. David, N.; Alpert, P.; Messer, H. The potential of cellular network infrastructures for sudden rainfall monitoring in dry climate regions. *Atmos. Res.* **2013**, *131*, 13–21. [[CrossRef](#)]
16. Dinku, T.; Anagnostou, E.N.; Borga, M. Improving radar-based estimation of rainfall over complex terrain. *J. Appl. Meteorol.* **2002**, *41*, 1163–1178. [[CrossRef](#)]
17. Hoedjes, J.C.B.; Kooiman, A.; Maathuis, B.H.P.; Said, M.Y.; Becht, R.; Limo, A.; Mumo, M.; Nduhiu-Mathenge, J.; Shaka, A.; Su, B. A Conceptual Flash Flood Early Warning System for Africa, Based on Terrestrial Microwave Links and Flash Flood Guidance. *ISPRS Int. J. Geo-Inf.* **2014**, *3*, 584–598. [[CrossRef](#)]
18. Rosenfeld, D. Cloud Top Microphysics as a Tool for Precipitation Measurements. In *Measuring Precipitation from Space*; Levizzani, V., Bauer, P., Turk, F.J., Eds.; Springer: Dordrecht, The Netherlands, 2007; Volume 1, pp. 61–77.
19. Kidd, C.; Levizzani, V.; Laviola, S.; Testik, F.Y.; Gebremichael, M. Section II: Rainfall Measurement and Estimation. In *Extreme Events*; American Geophysical Union (AGU): Washington, DC, USA, 2010; Volume 191, pp. 127–158.
20. Paredes, T.J.F.; Álvarez, B.H.; Peñaloza-Murillo, M.A.; Moreno, M.A.; Farias, A. Intercomparison of improved satellite rainfall estimation with CHIRPS gridded product and rain gauge data over Venezuela. *Atmósfera* **2016**, *29*, 323–342. [[CrossRef](#)]
21. Sohn, B.J.; Han, H.J.; Seo, E.K. Validation of satellite-based high-resolution rainfall products over the Korean Peninsula using data from a dense rain gauge network. *J. Appl. Meteorol. Climatol.* **2010**, *49*, 701–714. [[CrossRef](#)]
22. Dezfuli, A.K.; Ichoku, C.M.; Huffman, G.J.; Mohr, K.I.; Selker, J.S.; van de Giesen, N.; Hochreutener, R.; Annor, F.O. Validation of IMERG Precipitation in Africa. *J. Hydrometeorol.* **2017**, *18*, 2817–2825. [[CrossRef](#)]
23. Doumounia, A.; Gosset, M.; Cazenave, F.; Kacou, M.; Zougmore, F. Rainfall monitoring based on microwave links from cellular telecommunication networks: First results from a West African test bed. *Geophys. Res. Lett.* **2014**, *41*, 6016–6022. [[CrossRef](#)]
24. Chwala, C.; Gmeiner, A.; Qiu, W.; Hipp, S.; Nienaber, D.; Siart, U.; Eibert, T.; Pohl, M.; Selmann, J.; Fritz, J.; et al. Precipitation observation using microwave backhaul links in the alpine and pre-alpine region of Southern Germany. *Hydrol. Earth Syst. Sci.* **2012**, *16*, 2647–2661. [[CrossRef](#)]
25. Leijnse, H.; Uijlenhoet, R.; Stricker, J.N.M. Hydrometeorological Application Of A Microwave Link: 2. Precipitation. *Water Resour. Res.* **2007**, *43*, 1–9. [[CrossRef](#)]
26. Messer, H.; Zinevich, A.; Alpert, P. Environmental monitoring by wireless communication networks. *Science* **2006**, *312*, 713. [[CrossRef](#)] [[PubMed](#)]
27. Overeem, A.; Leijnse, H.; Uijlenhoet, R. Retrieval algorithm for rainfall mapping from microwave links in a cellular communication network. *Atmos. Meas. Tech.* **2016**, *9*, 2425–2444. [[CrossRef](#)]
28. Marielle, G.; Kunstmann, H.; Zougmore, F.; Cazenave, F.; Leijnse, H.; Uijlenhoet, R.; Chwala, C.; Keis, F.; Doumounia, A.; Boubacar, B.; et al. Improving Rainfall Measurement in Gauge Poor Regions Thanks to Mobile Telecommunication Networks. *Bull. Am. Meteorol. Soc.* **2016**, *97*, ES49–ES51. [[CrossRef](#)]
29. Uijlenhoet, R.; Overeem, A.; Leijnse, H. Opportunistic remote sensing of rainfall using microwave links from cellular communication networks. *Wires Water* **2018**, *5*. [[CrossRef](#)]
30. Chwala, C.; Kunstmann, H. Commercial microwave link networks for rainfall observation: Assessment of the current status and future challenges. *Wires Water* **2019**, *6*, e1337. [[CrossRef](#)]
31. Sebastianelli, S.; Russo, F.; Napolitano, F.; Baldini, L. On precipitation measurements collected by a weather radar and a rain gauge network. *Nat. Hazards Earth Syst. Sci.* **2013**, *13*, 605–623. [[CrossRef](#)]

32. Todini, E. A Bayesian technique for conditioning radar precipitation estimates to rain-gauge measurements. *Hydrol. Earth Syst. Sci.* **2001**, *5*, 187–199. [CrossRef]
33. Long, Y.; Zhang, Y.; Ma, Q. A Merging Framework for Rainfall Estimation at High Spatiotemporal Resolution for Distributed Hydrological Modeling in a Data-Scarce Area. *Remote Sens.* **2016**, *8*, 599. [CrossRef]
34. Bianchi, B.; Jan van Leeuwen, P.; Hogan, R.J.; Berne, A. A Variational Approach to Retrieve Rain Rate by Combining Information from Rain Gauges, Radars, and Microwave Links. *J. Hydrometeorol.* **2013**, *14*, 1897–1909. [CrossRef]
35. Liberman, Y.; Samuels, R.; Alpert, P.; Messer, H. New algorithm for integration between wireless microwave sensor network and radar for improved rainfall measurement and mapping. *Atmos. Meas. Tech.* **2014**, *7*, 3549–3563. [CrossRef]
36. Scheidegger, A.; Rieckermann, J. Bayesian Assimilation of Rainfall Sensors with Fundamentally Different Integration Characteristics. Available online: https://www.researchgate.net/publication/261586169_Bayesian_assimilation_of_rainfall_sensors_with_fundamentally_different_integration_characteristics (accessed on 16 August 2020).
37. Kühnlein, M.; Thies, B.; Nauß, T.; Bendix, J. Rainfall-Rate Assignment Using MSG SEVIRI Data—A Promising Approach to Spaceborne Rainfall-Rate Retrieval for Midlatitudes. *J. Appl. Meteorol. Climatol.* **2010**, *49*, 1477–1495. [CrossRef]
38. Thies, B.; Nauss, T.; Bendix, J. Discriminating raining from non-raining cloud areas at mid-latitudes using meteosat second generation SEVIRI night-time data. *Meteorol. Appl.* **2008**, *15*, 219–230. [CrossRef]
39. Thies, B.; Nauss, T.; Bendix, J. Discriminating raining from non-raining clouds at mid-latitudes using meteosat second generation daytime data. *Atmos. Chem. Phys.* **2008**, *8*, 2341–2349. [CrossRef]
40. Roebeling, R.A.; Holleman, I. SEVIRI rainfall retrieval and validation using weather radar observations. *J. Geophys. Res. Atmos.* **2009**, *114*, 1–13. [CrossRef]
41. Schip, v.h.T.I.; Overeem, A.; Leijnse, H.; Uijlenhoet, R.; Meirink, J.F.; van Delden, A.J. Rainfall measurement using cell phone links: Classification of wet and dry periods using geostationary satellites. *Hydrol. Sci. J.* **2017**, *62*, 1343–1353. [CrossRef]
42. Hoedjes, J.; Said, M.; Becht, R.; Kifugo, S.; Kooiman, A.; Limo, A.; Maathuis, B.; Moore, I.; Mumo, M.; Nduhiu Mathenge, J.; et al. Towards Near Real-time Convective Rainfall Observations over Kenya. *EGUGA 2013*, EGU2013-8082.
43. Kimani, M.W.; Hoedjes, J.C.B.; Su, Z. An assessment of satellite-derived rainfall products relative to ground observations over East Africa. *Remote Sens.* **2017**, *9*, 430. [CrossRef]
44. Schneider, T.; Bischoff, T.; Haug, G.H. Migrations and dynamics of the intertropical convergence zone. *Nature* **2014**, *513*, 45–53. [CrossRef]
45. MoAlf. *Climate Risk Profile for Kericho County*. Kenya County Climate Risk Profile Series; MoAlf: Nairobi, Kenya, 2017.
46. Odongo, V.O.; van der Tol, C.; van Oel, P.R.; Meins, F.M.; Becht, R.; Onyando, J.; Su, Z. Characterisation of hydroclimatological trends and variability in the Lake Naivasha basin, Kenya. *Hydrol. Process.* **2015**, *29*, 3276–3293. [CrossRef]
47. Kenya, R.O. *County Government of Kericho: Second Generation County Integrated Development Plan 2018–2022*; Kenya, R.O.: Nairobi, Kenya, 2017.
48. van de Giesen, N.; Hut, R.; Selker, J. The Trans-African Hydro-Meteorological Observatory (TAHMO). *Wiley Interdiscip. Rev. Water* **2014**, *1*, 341–348. [CrossRef]
49. EROS, U. USGS EROS Archive—Digital Elevation—Shuttle Radar Topography Mission (SRTM) 1 Arc-Second Global. Available online: https://www.usgs.gov/centers/eros/science/usgs-eros-archive-digital-elevation-shuttle-radar-topography-mission-srtm-1-arc?qt-science_center_objects=0#qt-science_center_objects (accessed on 28 April 2020).
50. Atlas, D.; Ulbrich, C.W. Path- and Area-Integrated Rainfall Measurement by Microwave Attenuation in the 1–3 cm Band. *J. Appl. Meteorol.* **1977**, *16*, 1322–1331. [CrossRef]
51. Zinevich, A.; Messer, H.; Alpert, P. Prediction of rainfall intensity measurement errors using commercial microwave communication links. *Atmos. Meas. Tech.* **2010**, *3*, 1385–1402. [CrossRef]
52. EUMETSAT. Meteosat Second Generation (MSG) Provides Images of the Full Earth disc, and Data for Weather Forecasts. Available online: <https://www.eumetsat.int/website/home/Satellites/CurrentSatellites/Meteosat/index.html> (accessed on 11 August 2020).

53. Eumetsat. Meteosat-8 Satellite's New Position of 41.5E Provides Weather and Climate View over the Indian Ocean. Available online: <https://phys.org/news/2016-09-meteosat-satellite-position-415e-weather.html> (accessed on 14 July 2020).
54. Schmetz, J.; Pili, P.; Tjemkes, S.; Just, D.; Kerkmann, J.; Rota, S.; Ratier, A. An Introduction to Meteosat Second Generation (MSG). *Bull. Am. Meteorol. Soc.* **2002**, *83*, 977–992. [\[CrossRef\]](#)
55. Maathuis, B.; Mannaerts, C.; Schouwenburg, M.; Retsios, B.; Lemmens, R. *GEONETCAST Toolbox: Installation, Configuration and User Guide of the Geonetcast Toolbox Plug-In for Ilwis 3.7*; University of Twente: Enschede, The Netherlands, 2014; pp. 1–143.
56. Bergès, J.C.; Chopin, F.; Bessat, F.; Based, S. Satellite Based Downscaling Algorithm for Rainfall Estimation Hal. In Proceedings of the IV Colóquio Brasileiro de Ciências Geodésicas—IV CBCG, Curitiba, Brazil, 16–20 May 2005.
57. Olsen, R.; Rogers, D.; Hodge, D. The aRb Relation in the Calculation of Rain Attenuation. *IEEE Trans. Antennas Propag.* **1978**, *26*, 318–329. [\[CrossRef\]](#)
58. Itu, R. *RECOMMENDATION ITU-R P.838-2 Specific Attenuation Model for Rain for Use in Prediction Methods*; 1992/1999/20032; ITU: Geneva, Switzerland, 2005; pp. 1–8.
59. Ostrometzky, J.; Messer, H. Accumulated Rainfall Estimation Using Maximum Attenuation of Microwave Radio Signal. In Proceedings of the 2014 IEEE 8th Sensor Array and Multichannel Signal Processing Workshop (SAM), A Coruna, Spain, 22–25 June 2014; pp. 193–196.
60. David, N.; Alpert, P.; Messer, H. Technical Note: Novel method for water vapour monitoring using wireless communication networks measurements. *Atmos. Chem. Phys.* **2009**, *9*, 2413–2418. [\[CrossRef\]](#)
61. David, N.; Gao, H.O. Using Cell-Phone Tower Signals for Detecting the Precursors of Fog. *J. Geophys. Res. Atmos.* **2018**, *123*, 1325–1338. [\[CrossRef\]](#)
62. Schleiss, M.; Berne, A. Identification of dry and rainy periods using telecommunication microwave links. *IEEE Geosci. Remote Sens. Lett.* **2010**, *7*, 611–615. [\[CrossRef\]](#)
63. Wang, Z.; Schleiss, M.; Jaffrain, J.; Berne, A.; Rieckermann, J. Using Markov switching models to infer dry and rainy periods from telecommunication microwave link signals. *Atmos. Meas. Tech.* **2012**, *5*, 1847–1859. [\[CrossRef\]](#)
64. Endris, H.S.; Omondi, P.; Jain, S.; Lennard, C.; Hewitson, B.; Chang'a, L.; Awange, J.L.; Dosio, A.; Ketiem, P.; Nikulin, G.; et al. Assessment of the Performance of CORDEX Regional Climate Models in Simulating East African Rainfall. *J. Clim.* **2013**, *26*, 8453–8475. [\[CrossRef\]](#)
65. Wakachala, F.M.; Shilenje, Z.W.; Nguyo, J.; Shaka, S.; Apondo, W. Statistical Patterns of Rainfall Variability in the Great Rift Valley of Kenya. *J. Environ. Agric. Sci.* **2015**, *5*, 17–26.
66. ITU. *ITU-R Attenuation by Atmospheric Gases and Related Effects*; ITU: Istanbul, Turkey, 2019.
67. Schleiss, M.; Rieckermann, J.; Berne, A. Quantification and modeling of wet-antenna attenuation for commercial microwave links. *IEEE Geosci. Remote Sens. Lett.* **2013**, *10*, 1195–1199. [\[CrossRef\]](#)
68. Thies, B.; Nauss, T.; Bendix, J. First results on a process-oriented rain area classification technique using Meteosat Second Generation SEVIRI nighttime data. *Adv. Geosci.* **2008**, *16*, 63–72. [\[CrossRef\]](#)
69. Lensky, I.M.; Rosenfeld, D. A night-rain delineation algorithm for infrared satellite data based on microphysical considerations. *J. Appl. Meteorol.* **2003**, *42*, 1218–1226. [\[CrossRef\]](#)
70. Thies, B.; Nauss, T.; Bendix, J. A new technique for detecting precipitation at mid-latitudes during daytime using Meteosat Second Generation SEVIRI. In Proceedings of the EUMETSAT Meteorological Satellite Conference, Darmstadt, Germany, 8–12 September 2008.
71. Lensky, I.M.; Rosenfeld, D. Satellite-based insights into precipitation formation processes in continental and maritime convective clouds at nighttime. *J. Appl. Meteorol.* **2003**, *42*, 1227–1233. [\[CrossRef\]](#)
72. Lazri, M.; Ameer, S.; Brucker, J.M.; Testud, J.; Hamadache, B.; Hameg, S.; Oualloche, F.; Mohia, Y. Identification of raining clouds using a method based on optical and microphysical cloud properties from Meteosat second generation daytime and nighttime data. *Appl. Water Sci.* **2013**, *3*, 1–11. [\[CrossRef\]](#)
73. Lazri, M.; Ameer, S.; Mohia, Y. Instantaneous rainfall estimation using neural network from multispectral observations of SEVIRI radiometer and its application in estimation of daily and monthly rainfall. *Adv. Space Res.* **2014**, *53*, 138–155. [\[CrossRef\]](#)
74. Feidas, H.; Giannakos, A. Identifying precipitating clouds in Greece using multispectral infrared Meteosat Second Generation satellite data. *Theor. Appl. Climatol.* **2011**, *104*, 25–42. [\[CrossRef\]](#)
75. Eumetsat. *Cloud Mask Product: Product Guide*; Eumetsat: Darmstadt, Germany, 2015; pp. 1–6.

76. Baum, B.A.; Spinhirne, J.D. Remote sensing of cloud properties using MODIS airborne simulator imagery during SUCCESS: 3. Cloud Overlap. *J. Geophys. Res. Atmos.* **2000**, *105*, 11793–11804. [\[CrossRef\]](#)
77. Kawamoto, K.; Nakajima, T.; Nakajima, T.Y. A global determination of cloud microphysics with AVHRR remote sensing. *J. Clim.* **2001**, *14*, 2054–2068. [\[CrossRef\]](#)
78. Kokhanovsky, A.A. A semianalytical cloud retrieval algorithm using backscattered radiation in 0.4–2.4 μm spectral region. *J. Geophys. Res.* **2003**, *108*. [\[CrossRef\]](#)
79. Thies, B.; Nauss, T. *A New Technique for Detecting Precipitation at Mid-Latitudes during Daytime Using Meteosat Second Generation SEVIRI*; Eumetsat: Darmstadt, Germany, 2008.
80. Thies, B.; Nauss, T.; Bendix, J. Precipitation process and rainfall intensity differentiation using Meteosat Second Generation Spinning Enhanced Visible and Infrared Imager data. *J. Geophys. Res. Atmos.* **2008**, *113*, D23206. [\[CrossRef\]](#)
81. Strabala, K.I.; Ackerman, S.A.; Menzel, W.P. Cloud Properties inferred from 8–12- μm Data. *J. Appl. Meteorol.* **1994**, *33*, 212–229. [\[CrossRef\]](#)
82. Wolters, E.L.A.; Roebeling, R.A.; Feijt, A.J. Evaluation of cloud-phase retrieval methods for SEVIRI on Meteosat-8 using ground-based lidar and cloud radar data. *J. Appl. Meteorol. Climatol.* **2008**, *47*, 1723–1738. [\[CrossRef\]](#)
83. Inoue, T. An Instantaneous Delineation of Convective Rainfall Areas Using Split Window Data of Noaa-7 Avhrr. *J. Meteorol. Soc. Jpn.* **1987**, *65*, 469–481. [\[CrossRef\]](#)
84. Feidas, H.; Giannakos, A. Classifying convective and stratiform rain using multispectral infrared Meteosat Second Generation satellite data. *Theor. Appl. Climatol.* **2011**, *108*, 613–630. [\[CrossRef\]](#)
85. Inoue, T.; Wu, X.; Bessho, K. Life Cycle of Convective Activity in Terms of Cloud Type Observed By Split Window. In Proceedings of the 11th Conference on Satellite Meteorology and Oceanography, Madison, WI, USA, 16 October 2001; pp. 3–4.
86. Inoue, T. Day-to-night cloudiness change of cloud types inferred from split window measurements aboard NOAA polar-orbiting satellites. *J. Meteorol. Soc. Jpn.* **1997**, *75*, 59–66. [\[CrossRef\]](#)
87. Ha, E.; North, G.R.; Yoo, C.; Ha, K.J. Evaluation of some ground truth designs for satellite estimates of rain rate. *J. Atmos. Ocean. Technol.* **2002**, *19*, 65–73. [\[CrossRef\]](#)
88. Roe, G.H. Orographic precipitation. *Annu. Rev. Earth Planet. Sci.* **2005**, *33*, 645–671. [\[CrossRef\]](#)
89. Young, A.H.; Bates, J.J.; Curry, J.A. Application of cloud vertical structure from CloudSat to investigate MODIS-derived cloud properties of cirriform, anvil, and deep convective clouds. *J. Geophys. Res. Atmos.* **2013**, *118*, 4689–4699. [\[CrossRef\]](#)
90. Kato, S.; Marshak, A. Solar zenith and viewing geometry-dependent errors in satellite retrieved cloud optical thickness: Marine stratocumulus case. *J. Geophys. Res. Atmos.* **2009**, *114*, 1–13. [\[CrossRef\]](#)
91. Cattani, E.; Torricella, F.; Laviola, S.; Levizzani, V. On the statistical relationship between cloud optical and microphysical characteristics and rainfall intensity for convective storms over the Mediterranean. *Nat. Hazards Earth Syst. Sci.* **2009**, *9*, 2135–2142. [\[CrossRef\]](#)
92. Walther, B.A.; Moore, J.L. The concepts a literature with of species richness the performance estimators, of estimator review performance precision. *Ecography* **2005**, *28*, 815–829. [\[CrossRef\]](#)
93. Wilks, D.S. *Statistical Methods in the Atmospheric Sciences*; Academic Press: Cambridge, MA, USA, 2006; Volume 14, p. 627.
94. Barnston, A.G. Correspondence among the Correlation, RMSE, and Heidke Forecast Verification Measures; Refinement of the Heidke Score. *Weather Forecast.* **1992**, *7*, 699–709. [\[CrossRef\]](#)
95. Harold, B.; Barb, B.; Beth, E.; Chris, F.; Johannes, J.; Ian, J.; Tieh-Yong, K.; Paul, R.; David, S. *WWRP/WGNE Joint Working Group on Forecast Verification Research*; WMO: Geneva, Switzerland, 2015.
96. Inoue, T.; Vila, D.; Rajendran, K.; Hamada, A.; Wu, X.Q.; Machado, L.A.T. Life Cycle of Deep Convective Systems over the Eastern Tropical Pacific Observed by TRMM and GOES-W. *J. Meteorol. Soc. Jpn.* **2009**, *87a*, 381–391. [\[CrossRef\]](#)
97. Leijnse, H.; Uijlenhoet, R.; Berne, A. Errors and Uncertainties in Microwave Link Rainfall Estimation Explored Using Drop Size Measurements and High-Resolution Radar Data. *J. Hydrometeorol.* **2010**, *11*, 1330–1344. [\[CrossRef\]](#)
98. Leijnse, H.; Uijlenhoet, R.; Stricker, J.N.M. Microwave link rainfall estimation: Effects of link length and frequency, temporal sampling, power resolution, and wet antenna attenuation. *Adv. Water Resour.* **2008**, *31*, 1481–1493. [\[CrossRef\]](#)

99. Martin, F.; Vojtech, B. Quantifying Hardware Related Attenuation from the Analysis of Nearby Microwave Links. In Proceedings of the 2018 IEEE Workshop on Statistical Signal Processing (SSP), Freiburg, Germany, 10–13 June 2018; pp. 135–138.
100. David, N.; Gao, H.O.; Kumah, K.K.; Hoedjes, J.C.B.; Su, Z.; Liu, Y. Microwave communication networks as a sustainable tool of rainfall monitoring for agriculture needs in Africa. In Proceedings of the 16th International Conference on Environmental Science and Technology, Rhodes, Greece, 4–7 September 2019.
101. Safont, G.; Salazar, A.; Vergara, L. Multiclass Alpha Integration of Scores from Multiple Classifiers. *Neural Comput.* **2019**, *31*, 806–825. [\[CrossRef\]](#)
102. Lahat, D.; Adali, T.; Jutten, C. Multimodal Data Fusion: An Overview of Methods, Challenges, and Prospects. *Proc. IEEE* **2015**, *103*, 1449–1477. [\[CrossRef\]](#)
103. Kühnlein, M.; Appelhans, T.; Thies, B.; Nauß, T. Precipitation Estimates from MSG SEVIRI Daytime, Nighttime, and Twilight Data with Random Forests. *J. Appl. Meteorol. Climatol.* **2014**, *53*, 2457–2480. [\[CrossRef\]](#)
104. Meyer, H.; Kühnlein, M.; Appelhans, T.; Nauss, T. Comparison of four machine learning algorithms for their applicability in satellite-based optical rainfall retrievals. *Atmos. Res.* **2016**, *169*, 424–433. [\[CrossRef\]](#)
105. Watts, P.D.; Bennartz, R.; Fell, F. Retrieval of two-layer cloud properties from multispectral observations using optimal estimation. *J. Geophys. Res. Atmos.* **2011**, *116*, 1–22. [\[CrossRef\]](#)
106. Lensky, I.; Rosenfeld, D. Estimation of Precipitation Area and Rain Intensity Based on the Microphysical Properties Retrieved from NOAA AVHRR Data. *J. Appl. Meteorol.* **1997**, *36*, 234–242. [\[CrossRef\]](#)
107. Wang, J.Y.; Houze, R.A.; Fan, J.W.; Brodzik, S.R.; Feng, Z.; Hardin, J.C. The Detection of Mesoscale Convective Systems by the GPM Ku-Band Spaceborne Radar. *J. Meteorol. Soc. Jpn.* **2019**, *97*, 1059–1073. [\[CrossRef\]](#)
108. Zipser, E.J.; Cecil, D.J.; Liu, C.; Nesbitt, S.W.; Yorty, D.P. Where Are the Most Intense Thunderstorms on Earth? *Bull. Am. Meteorol. Soc.* **2006**, *87*, 1057–1072. [\[CrossRef\]](#)
109. Kober, K.; Tafferner, A. Tracking and nowcasting of convective cells using remote sensing data from radar and satellite. *Meteorol. Z.* **2009**, *18*, 75–84. [\[CrossRef\]](#)
110. Turdukulov, U.D.; Kraak, M.J.; Blok, C.A. Designing a visual environment for exploration of time series of remote sensing data: In search for convective clouds. *Comput. Graph.* **2007**, *31*, 370–379. [\[CrossRef\]](#)
111. Bell, T.L.; Kundu, P.K. Comparing satellite rainfall estimates with rain gauge data: Optimal strategies suggested by a spectral model. *J. Geophys. Res. Atmos.* **2003**, *108*. [\[CrossRef\]](#)
112. Kühnlein, M.; Appelhans, T.; Thies, B.; Nauss, T. Improving the accuracy of rainfall rates from optical satellite sensors with machine learning—A random forests-based approach applied to MSG SEVIRI. *Remote Sens. Environ.* **2014**, *141*, 129–143. [\[CrossRef\]](#)

